



UNIVERSITY OF AMSTERDAM

FACULTY OF SCIENCE

Van der Waals–Zeeman Institute

Optical gain measurements on oxidized amorphous silicon nitride

Report of Bachelorproject Physics and Astronomy, size 12 EC, completed in the period
09-05-2011 to 29-07-2011

Author:

Leon WEBBERS

Supervisor:

Dr. Katerina DOHNALOVÁ

Student number:

5967716

Second reviewer:

Prof. Dr. Tom GREGORKIEWICZ

August 9, 2011

Abstract

Currently there is an ongoing search for a way to create an efficient silicon-based light source; in particular, a cost-effective Si-based laser which can be integrated directly into existing microchip technology. The aim of this work is to contribute to this quest by investigating the optical properties of six different samples of oxidized amorphous silicon nitride ($a\text{-SiO}_x\text{N}_y$) and to verify the presence of optical gain. The samples were prepared using two different ratios of $\text{SiH}_4:\text{NH}_3$ and three different waveguide structures, and investigated both in a standard PL setup and using a combination of the variable stripe length and shifting excitation spot techniques. When comparing the influence of the composition on the PL properties, power dependence measurements indicate that the presence of extra nitrogen leads to slower decay times and to strong saturation behavior. Results from the optical gain measurements indicate that the broad 1D waveguide structure ‘b’ is the most suitable for optical applications, as the N-rich sample with this structure shows optical gain of at least 6 cm^{-1} . However, to verify this result and to exclude waveguiding effects as the source of the gain, additional research—or at the least a re-examination of this sample—is advised.

Populair wetenschappelijke samenvatting

Tegenwoordig nemen computers een steeds belangrijkere rol in onze samenleving in. Zo verlopen zaken als het aanmelden voor academische vakken en communicatie met docenten veelal via het internet, met behulp van een computer, smartphone of tablet. Communicatie tussen de verschillende componenten op een computerchip en tussen verschillende chips onderling vindt momenteel plaats via elektriciteit. Elektronen, dragers van elektrische lading, zijn verantwoordelijk voor deze informatieoverdracht. Het gebruik hiervan brengt echter een aantal beperkingen met zich mee. Een logische stap is dan ook om op zoek te gaan naar een medium voor informatieoverdracht dat deze beperkingen niet of in mindere mate heeft. Licht is zo'n medium.

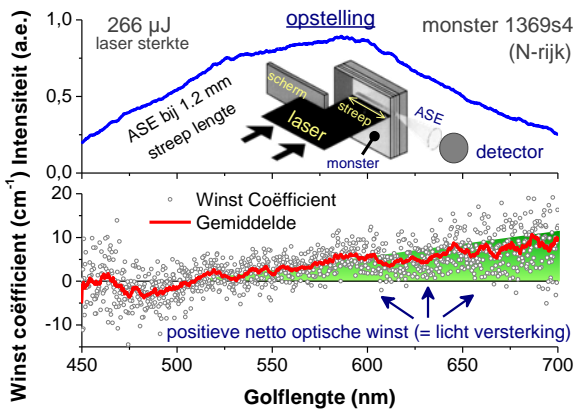
Het gebruik van licht biedt een aantal belangrijke voordelen met betrekking tot snelheid en benodigde ruimte ten opzichte van elektriciteit. Verder is de integratie in zogenaamde 'human interface devices' zoals beeldschermen, alsmede in specifieke toepassingen zoals biologische sensoren, een stuk eenvoudiger en zijn de energiebehoeften lager. Waarom wordt dit dan nog niet overal toegepast? Het probleem is dat het integreren van optische functionaliteit in bestaande, op silicium (Si) gebaseerde, toepassingen erg lastig blijkt.

Naar de toepassing van Si in lasers en gerelateerde optische componenten is veel onderzoek verricht, zowel in wetenschappelijke als in commerciële kring (denk hierbij aan bedrijven zoals Intel en IBM). Om een Si laser te kunnen bouwen, is naast de directe uitzending van licht—fotoluminescentie (FL)—vanaf een siliciumchip ook *gestimuleerde emissie* nodig. Dit is een proces waarbij, simpel gezegd, door toedoen van invallend licht nieuw licht wordt uitgezonden, dat dezelfde kenmerken heeft als het invallende licht. Er treedt dus versterking op van licht, iets wat ook wel *optische winst* wordt genoemd. Dit is helaas in veel materialen, waaronder in puur Si, moeilijk te bereiken omdat er naast winst ook veel verlies kan zijn.

Alleen als de winst de verliezen overstijgt, is er ook daadwerkelijk sprake van versterking van licht (netto winst). Omdat dit, zoals gezegd, in puur Si zoals je dat vindt in een chip lastig te bereiken is, is men momenteel allerlei samengestelde materialen met Si, evenals speciale structuren (zoals Si nanokristallen¹) aan het onderzoeken. Voor deze scriptie is een materiaal onderzocht dat *geoxideerd amorf silicium nitride* ($a\text{-SiO}_x\text{N}_y$) heet. Dit is een amorfe (d. w. z. glasachtige) substantie die bestaat uit een variabele hoeveelheid silicium, zuurstof en stikstof, en die als voordeel heeft dat ze direct in een chip kan worden geïntegreerd.

Tijdens het onderzoek is gekeken naar verschillende monsters, die allemaal een iets andere samenstelling of structuur hadden. De monsters zijn één voor één belicht met een laserstraal in een zelfgebouwde opstelling en er is gekeken naar het licht dat er vervolgens vanaf kwam. Hierbij is voor elk monster gekeken naar het spectrum ('hoeveel licht komt er van af en welke golflengtes heeft het?'), de afhankelijkheid van de FL van het vermogen van de laser ('wat gebeurt er wanneer ik het vermogen van de laser opvoer?'), de tijdsafhankelijkheid van de FL ('hoe verandert de intensiteit van het uitgezonden licht met de tijd?') en de aanwezigheid van optische winst. Op basis van de eerste drie metingen kan worden vastgesteld wat de bron van de FL is, terwijl de laatste meting de geschiktheid voor eerdergenoemde toepassingen kan aangeven.

Uit het onderzoek is gebleken dat de structuur van het materiaal een grote, en de samenstelling een wat minder grote invloed heeft op de optische eigenschappen. Bij één bepaalde combinatie van structuur en samenstelling is netto winst gemeten (zie Winst Coëfficient in de figuur hier-naast), hetgeen na verificatie wellicht zou kunnen leiden tot een toepassing in de eerste werkende op Si gebaseerde laser.



¹Een nanokristal is een kristal met een diameter ongeveer tienduizend keer kleiner dan die van een haar. Doordat deze kristallen zo klein zijn hebben ze speciale eigenschappen

Contents

1	Introduction	1
2	Theoretical background	2
2.1	Stimulated emission in silicon-based materials	2
2.2	Variable stripe length method	4
2.2.1	Limitations and gain-like artifacts	5
2.3	Shifting excitation spot method	6
3	Experimental approach	7
3.1	Photoluminescence experiments	7
3.1.1	Experimental setup	7
3.1.2	Measuring the power dependence	8
3.1.3	Measuring the time dependence	9
3.2	Optical gain experiments	9
3.2.1	Experimental setup	9
3.2.2	Measuring VSL and SES	10
4	Results and discussion	11
4.1	Photoluminescence experiments	11
4.1.1	Power dependence	12
4.1.2	Time dependence	13
4.2	Optical gain experiments	14
4.2.1	Rhodamine 6G	14
4.2.2	Sample 1401s1	16
4.2.3	Sample 1402s2	17
4.2.4	Sample 1369s2	18
4.2.5	Sample 1369s4	18
4.2.6	Sample 1374s2	20
4.2.7	Sample 1374s4	21
5	Conclusion	22
Acknowledgments & References		23
A	Optical Gain Analysis Toolkit	25
A.1	Main toolkit dialog	25
A.1.1	General parameters	25
A.1.2	Pre-/Post-processing	27
A.1.3	Smooth data	27
A.1.4	Reduce data	28
A.1.5	Normalize data	29
A.1.6	Integrate data	30
A.1.7	Sheet math	30
A.1.8	Find & plot specific column	30
A.1.9	Contour plot	31
A.1.10	Sheet deleter	31
A.2	Import auto-processing dialog	32
A.3	Worksheets auto-processing dialog	33

1 Introduction

In the field of optoelectronics, much time and effort has been invested in the search for an efficient silicon-based light source². The main goal has always been to find an energy-efficient and cost-effective solution for integrating optical functionality into existing semiconductor technologies (i. e. ‘laser-on-a-chip’). Companies like Intel and IBM are particularly active in this area. Current applications make use of direct band gap compound semiconductors, but a monolithic solution is preferable because of issues inherent in the interface of compound solutions (i. e. trapping of carriers on defects at the interface). If it can be found, such a solution could revolutionize the electronic industry, which is quickly reaching the limits of existing technology.

Using an integrated Si-based light source in electronic circuitry (e. g. for transferring information between two microchips) has several advantages over existing solutions; it does not suffer from the same limitations with regards to speed and use of space, it is easy to integrate into human interface devices such as displays and specific applications such as biological sensors, the power consumption is generally lower, and it is cheaper to boot [1]. Unfortunately, silicon happens to have an indirect band gap, which means it is not very well suited for optical applications.

The key to developing an efficient Si-based light source lies in reaching stimulated emission. In order to do that, a material has to be able to amplify light, i. e. there has to be *optical gain*. In bulk Si, several processes (which will be discussed in detail in the next section) severely inhibit the possibility of light amplification. In order to overcome this limitation, one has to either create a special structure or add other elements to the mix. It has been shown[2] that nanostructures—in particular *nanocrystals*—might be the answer to the problem. Research in this area was spearheaded by Pavesi et al., who claimed to have discovered optical gain in a system of quantum dots dispersed in a silicon dioxide (SiO_2) matrix [3].

However, in the quest for a silicon-based laser, many types of structures have been researched, including porous silicon (π -Si) and amorphous silicon (α -Si, or a-Si). Huang et al. have been investigating the optical properties of a particular type of a-Si, called *oxidized amorphous silicon nitride* (a-SiN:O , or $\text{a-SiO}_x\text{N}_y$) [4, 5, 6]. The advantages of this material include strong, tunable, photoluminescence (PL) and a potential barrier lower than that of silicon dioxide (SiO_2). Because of this low potential barrier, the injection efficiency of carriers within this material could potentially be higher than that found in Si nanocrystals. Another significant advantage of this material is that it is CMOS compatible, facilitating direct integration with existing microchip technology.

Currently, the group of Huang et al. is investigating the influence of different structures and compositions on the optical properties of $\text{a-SiO}_x\text{N}_y$. The aim of this project is to contribute to this investigation by looking at the optical properties of six different samples of this material. In particular, we hope to discover optical gain on one or more of these samples, which were provided to us by the State Key Laboratory of Solid State Microstructures of the Nanjing University in China. The samples were prepared using the method described in [4], with two different ratios of the constituent gases and two different waveguide structures. The different compositions and structures are detailed in Table 1 and illustrated in Figure 1.1.

Sample ID	Ratio $\text{SiH}_4:\text{NH}_3$	Waveguide structure
1401s1	1:4	—
1402s2	1:1	—
1369s2	1:4	(a)
1369s4	1:4	(b)
1374s2	1:1	(a)
1374s4	1:1	(b)

Table 1: List of samples, detailing composition and structure.

²As a measure of the interest in this topic, the August 2010 issue of Nature Photonics, for example, was entirely dedicated to silicon photonics

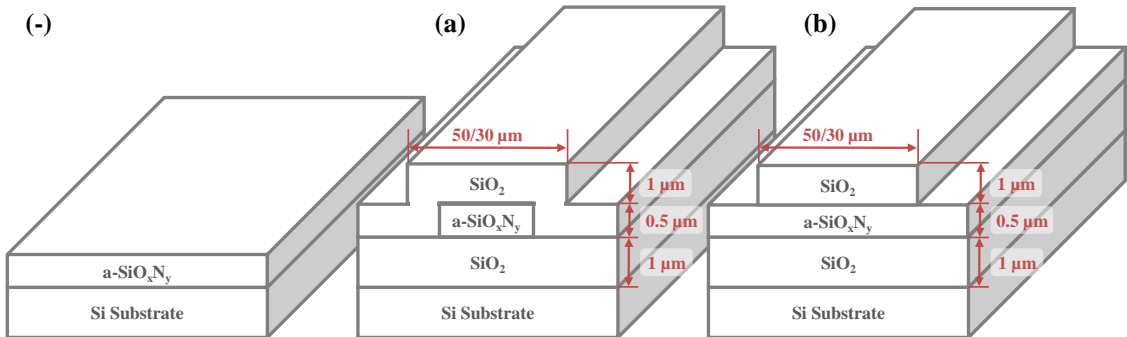


Figure 1.1: Schematic representation of the sample structures. All of the samples were 1 cm wide and 2 cm long.

To investigate the optical properties of this material, we will first have a look at the dependence of the PL obtained from samples 1401s1 and 1402s2 on the excitation beam power. This will provide an early indication for the possibility of finding optical gain, and we will see what kind of effect the different ratios of silicon/oxygen and nitrogen in these samples will have. For example, a fairly recent study[7] suggested that oxide passivation plays an important role in providing optical gain from silicon nanocrystals. Through our experiments we will be able to verify whether this is also the case for optical gain in a-SiO_xN_y.

For these samples we will also look at the time-dependence of the PL, in order to determine the origin of the luminescence. Next, we will investigate both the samples with 2D and those with 1D waveguide structures, using a combination of the variable stripe length (VSL) and shifting excitation spot (SES) techniques, in order to determine the influence of different structures and compositions on the presence of optical gain.

Details about the aforementioned techniques and their limitations will be made clear in the next section, followed by a description of our experimental approach in section 3. After that, we will present our results and discuss them in section 4 and finally conclude in section 5. In appendix A we have included a detailed description of a piece of software developed during the project and used for processing our experimental data.

2 Theoretical background

In this section, we will present the theoretical knowledge necessary to explain the reasoning behind, and development of, the methods used in this report. We will start with a short introduction into the theory of photoluminescence and stimulated emission in silicon-based materials, followed by a discussion of the variable stripe length method, its applicability and limitations, and end with a description of the shifting excitation spot technique.

2.1 Stimulated emission in silicon-based materials

Stimulated emission is one of the three ways in which light can interact with matter. The other two are: absorption and spontaneous emission. Stimulated emission can occur when a photon passes through a system with an inverted population³ such that, instead of being absorbed, it causes an excited carrier to drop back down to a lower energy level. This causes the system to emit a photon with the exact same characteristics as the one which triggered the emission. In essence, this transition can be viewed as a kind of reversed absorption and, as is the case for absorption,

³Population inversion occurs whenever there are more excited carriers than non-excited ones present in a system (in the language of band theory: whenever there are more electrons at the bottom of the conduction band than there are at the top of the valence band). This can be caused for example by optically pumping the system with a laser beam.

it can only occur in the presence of resonant states. Since the original photon remains intact, this means that there are *two* photons exiting the system, unlike during spontaneous emission. Hence, we have amplification of light, or *optical gain*.

The situation described above, while accurate for a system consisting of only two energy levels, one carrier and one photon, does not take into account the many things that complicate stimulated emission and light amplification in a real-life situation. In most cases, there are many processes competing with each other, limiting a system's potential for optical gain. For example, the extra photon emitted by one atom through stimulated emission, might be re-absorbed by the next atom it passes. As such, optical gain is a trade-off between losses and stimulated emission, and we can distinguish three situations: the losses are greater than the gain, the gain is greater than the losses, or the gain equals the losses (see also section 2.2). Only in the middle case can we speak of actual light amplification.

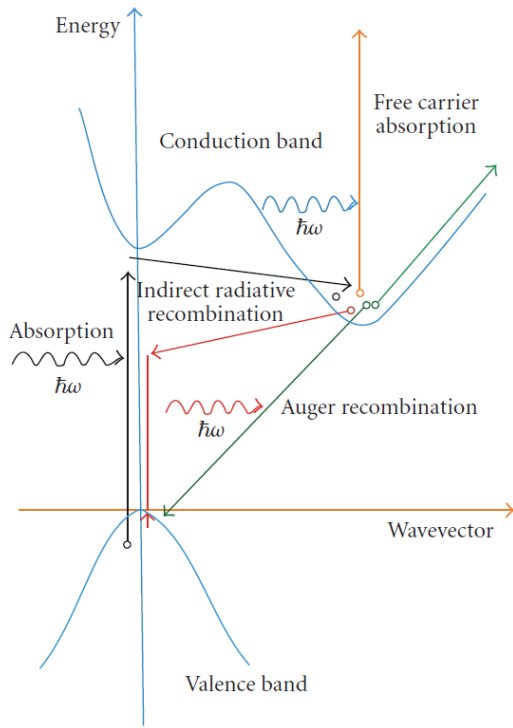


Figure 2.1: Band structure of bulk Si with various possible transitions for an electron-hole pair: radiative recombination, Auger recombination, and free-carrier absorption. [1]

In an indirect band gap semiconductor such as silicon, the situation is complicated further by the fact that additional momentum is required for an electron to cross the gap between energy-levels. Since photons alone carry very little momentum, a so-called *phonon* (lattice vibration) is required to close the gap in momenta between levels. However, the electron–phonon interaction is weak, so this kind of indirect radiative recombination does not take place on its own very easily (i.e. it is *strongly suppressed*) [8]. Still, the probability of a direct (unassisted) radiative recombination is even lower.

In contrast, the non-radiative recombinations happen much more easily. This is reflected in the lifetimes; radiative lifetimes are usually of the order of a few milliseconds, while non-radiative lifetimes are much shorter, of the order of a few nanoseconds [1]. This means that non-radiative processes rapidly deplete the excited carriers; hence the poor luminescence of (bulk-) silicon. It should come as no surprise then to learn that the dominant process in bulk Si turns out to be a non-radiative three-particle recombination mechanism called *Auger recombination* [1]. This mechanism is especially relevant when considering the use of Si as a gain-medium, because it

becomes more effective as more carriers are excited.

Yet another mechanism hampering light amplification in Si is the so-called *free carrier absorption* (also called *confined carrier absorption* in confined systems, such as Si nanocrystals) [1]. In this process, an excited carrier absorbs a photon, depleting the inverted population (i.e. the number of excited carriers) and increasing optical losses. Figure 2.1 illustrates the various competing processes in bulk Si that have been discussed so far.

As stated in the introduction, people have investigated the optical properties of many Si-based materials. One of the key discoveries during these investigations was that of visible-range emission from nanocrystalline and porous Si in the early 1990s [8]. This result suggested that the special properties of nanoscale materials might be able to overcome the limitations of bulk Si, especially when hosted in a dielectric matrix like SiO_2 . This discovery led to the formulation of the quantum confinement model and later to the vibron model (which describes the role of surface states).⁴ Quantum confinement increases the chances for radiative recombination to take place, while the surface chemistry in nanocrystalline Si is such that non-radiative recombination is suppressed. Thus the PL properties of nanocrystalline and porous Si are fairly well understood and, with respect to applications requiring light amplification, are superior to those of bulk Si.

However, when it comes to materials based on amorphous Si, not much is known about the mechanisms involved in PL. It is clear, though, that Si–O bonds at the surface interface between a-Si and SiO_2 play an important role [9], and since Si nanocrystals are often formed inside an a- SiO_x matrix, a further understanding of the properties of these materials could shed some more light on the problem of creating a laser out of Si.

2.2 Variable stripe length method

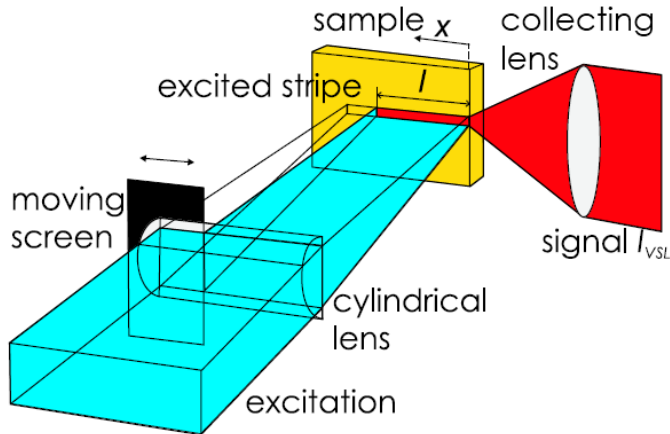


Figure 2.2: Illustration of the VSL method. [10]

In order to determine a material's potential for light amplification, the VSL method was developed. In this technique (illustrated in Fig. 2.2), a laser beam is focused on a sample through a moving screen using a cylindrical lens to create a stripe of variable length. The light emitted by the sample is collected from the side by a lens and passed to a detector. Thus the VSL technique can be viewed as a kind of *pump & probe* method where the spontaneous emission itself plays the role of the testing beam [10]. However, it can only be applied for excitation wavelengths where the spontaneous emission (SpE) is strong enough. As soon as population inversion is induced in the sample, it will act as a single-pass amplifier for light [11]. The net optical gain $G(\lambda)$ is then defined as the relative change in light intensity $dI(x, \lambda)$ at wavelength λ passing an infinitesimal distance dx along the stripe:

⁴For more details about the origin of PL in silicon nanostructures, including detailed descriptions of the quantum confinement model and the role of surface chemistry, see for example [9]

$$G(\lambda) = \frac{1}{I(x, \lambda)} \frac{dI(x, \lambda)}{dx} = g(\lambda) - K,$$

where $g(\lambda) = -\alpha$ is the material gain coefficient (defined as the negative absorption coefficient α of the material) and K is a parameter representing losses.

The total increment of detected light intensity $dI_{VSL}(x, \lambda)$ when increasing the stripe length x by a distance dx is determined by the sum of the spontaneous emission $I_{SpE}(\lambda)$ and the amplified spontaneous emission (ASE) [10]. This can be written as a differential equation involving the net optical gain coefficient:

$$dI_{VSL}(x, \lambda) = I_{SpE}(\lambda)dx + G(\lambda)I_{VSL}(x, \lambda)dx.$$

By integrating this equation over the whole stripe length (i.e. over x from 0 to l), we obtain the classical VSL equation

$$I_{VSL}(l, \lambda) = I_{SpE}(\lambda) \frac{e^{G(\lambda)l} - 1}{G(\lambda)}. \quad (1)$$

Here, it is usually assumed that $I_{SpE}(\lambda)$ and $G(\lambda)$ are independent of x and that coupling of the emission to the detector is constant [11]. Furthermore, we take the width of the stripe to be infinitely small.

From equation (1), we can get the net gain coefficient as a function of λ either through a direct fit, or by taking $I_{VSL}(2l, \lambda)$, dividing this by $I_{VSL}(l, \lambda)$ and solving the result $(e^{G(\lambda)l} + 1)$ for $G(\lambda)$:

$$G(\lambda) = \frac{1}{l} \ln \left(\frac{I_{VSL}(2l, \lambda)}{I_{VSL}(l, \lambda)} - 1 \right). \quad (2)$$

Only when $G(\lambda_0) > 0$ for a certain wavelength λ_0 can we speak of actual light amplification, for in this case $g(\lambda_0) > K$ (i.e. the gain is greater than the losses).

Another way to obtain the net gain coefficient, is by looking at spectral narrowing; since optical gain depends on the wavelength, the spectrum of amplified light should be narrower than that of scattered light from the same source [12]. Assuming the emission spectrum is approximately Gaussian in shape, we can use the equation

$$\Delta\nu_{ASE} = \Delta\nu_0 \sqrt{\frac{G(\lambda) - 1}{G(\lambda) \ln G(\lambda)}} \quad (3)$$

given in [13] to calculate the gain coefficient. In this equation, $\Delta\nu_{ASE}$ stands for the ASE linewidth, while $\Delta\nu_0$ is the transition linewidth. For our purposes, we can take $\Delta\nu_{ASE}$ to be the FWHM of the ASE spectrum (i.e. $I_{VSL}(l, \lambda)$) and $\Delta\nu_0$ as the FWHM of the SpE spectrum (i.e. $I_{VSL}(\sim 0, \lambda)$).

2.2.1 Limitations and gain-like artifacts

The VSL method and gain calculations based on the classical VSL equation work fine within their established boundaries and under certain conditions. However problems arise as soon as these conditions are not met. These problems and the applicability of the VSL method are examined in detail in [14] and will be summarized here.

Gain saturation The first problems arise when the conditions listed in the previous section for the derivation of equation (1) are not met. In general, the assumption that G is independent of x does not hold, because of the gain saturation effect. This effect occurs when the intensity of the ASE along the stripe depletes the excited state population, reducing or even completely canceling out population inversion. If this is the case, one would observe positive gain for small stripe lengths, which would decrease with increasing stripe length. However, as long as measurements are carried out within the so-called *saturation length* (i.e. the stripe length at which G vanishes), equation (1) is valid.

Pump diffraction effects The assumption that I_{SpE} is independent of x does not in general hold either. Not only is it difficult to create a perfectly homogeneous pump beam profile, assuming of course that the sample itself is perfectly homogeneous, but even under the best of circumstances the moving screen can cause *Fresnel diffraction*. Due to this effect, an increase in the ASE intensity can be observed that is not because of optical gain, but rather because of a local increase in the excitation beam intensity. However, this effect can be minimized by careful arrangement of the experimental setup, and because it does not depend either on pump power or on wavelength—unlike real optical gain—it is usually easy to identify and to take into account when processing experimental data.

Coupling effects The third assumption, that of constant coupling of the emission to the detector, does not always hold true either. Most importantly, this assumption does not hold in the case of planar waveguides. Because of waveguiding effects, light is emitted from the sample edge at a certain solid angle, so coupling with the detection system depends strongly on the numerical aperture (NA) of the collecting lens. Furthermore, because of the confocal effect, which can occur in measurements with longer excitation stripes when the focal point of the collecting lens is not at the edge of the sample but inside it, there is additional dependence on the numerical aperture. To increase the focus depth, the NA has to be made smaller, however, this decreases detector efficiency, especially when dealing with waveguides. To reduce artifacts caused by inhomogeneous coupling to the detector, the SES technique can be applied, as described in section 2.3.

Additionally, the presence of so-called *leaky modes* in waveguides, where some of the light leaks into the substrate, can strongly influence the VSL signal [12]. Waveguiding effects can also cause spectral narrowing and might thus easily be mistaken for optical gain. *Internal reflections* form another factor that is not taken into account by the VSL method. These can occur, for instance, when the stripe width is not negligible [10]. Finally, one has to take into account various gain-like artifacts with other causes than those described here. For example, if the sample is excited at a too high intensity, burning can occur, which can cause strong absorption and change the chemical composition of the sample. Of course, human error also remains an issue...

2.3 Shifting excitation spot method

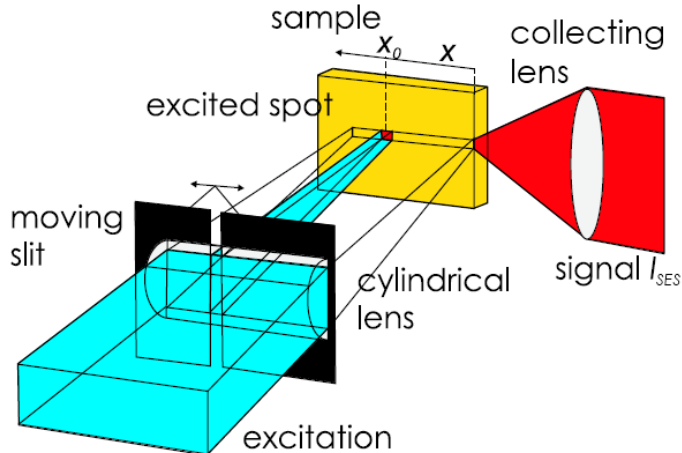


Figure 2.3: Illustration of the SES method. [10]

In order to correct for most of the artifacts and effects outlined in the previous section, the SES technique was developed [11]. This technique is very similar to the VSL technique described in the previous section, except that the moving screen is replaced by a moving slit (see Figure 2.3).

This causes only a tiny spot of the earlier stripe to be illuminated at a time. The spot size is chosen to be small enough so that stimulated emission does not occur. Aside from this, all the characteristics that would influence VSL measurements, such as inhomogeneity of the sample, confocal, or waveguiding effects, will still be present in the output signal. Thus by comparing VSL and SES measurements, most of the aforementioned artifacts can be identified and corrected for.

The total increment of detected light intensity $dI_{\text{SES}}(x, \lambda)$ when increasing the spot position x (as measured from the sample edge) by a distance dx is determined solely by the spontaneous emission $I_{\text{SpE}}(\lambda)$ [10]. This can be written as a differential equation,

$$dI_{\text{SES}}(x, \lambda) = I_{\text{SpE}}(\lambda) e^{-L(\lambda)x} dx,$$

where $L(\lambda) = \alpha_r(\lambda) + K$ represents the total optical losses in terms of the residual attenuation coefficient $\alpha_r(\lambda)$ and the parameter K introduced before. By integrating this equation over the whole stripe length (i.e. over x from 0 to l), we obtain the SES equation

$$I_{\text{SES}}(l, \lambda) = I_{\text{SpE}}(\lambda) \frac{1 - e^{L(\lambda)l}}{L(\lambda)}. \quad (4)$$

If no amplification due to stimulated emission is present, $I_{\text{SES}}(l, \lambda)$ must be equal to $I_{\text{VSL}}(l, \lambda)$ (e.g. for small stripe length). However, if we do have stimulated emission, $I_{\text{VSL}}(l, \lambda)$ should be greater than $I_{\text{SES}}(l, \lambda)$. Thus by subtracting the two signals, it is possible to make an accurate determination of the presence of optical gain. In practice, the quantity that is measured during SES experiments is $dI_{\text{SES}}(x, \lambda)$, in contrast to the direct measurement of $I_{\text{VSL}}(l, \lambda)$ during VSL experiments. This means that SES data have to be integrated numerically. As such, special care needs to be taken to ensure that no spot on the sample is counted twice or not counted at all, i.e. when probing the stripe, the slit must be moved in such a way that the spot excited on the sample covers an area that is exactly adjacent to the area previously probed. If this condition cannot be achieved, the SES data will have to be corrected manually after integration.

To prove beyond doubt that a material displays true gain (i.e. light amplification) at a certain wavelength λ_0 , it has to display the following characteristics:

- $I_{\text{VSL}}(l, \lambda_0) - \int_0^l dI_{\text{SES}}(x, \lambda_0) dx > 0$. Depending on the order of VSL and SES measurements, false positives can still occur due to e.g. burning or issues with the experimental setup.
- $G(\lambda_0) > 0$, both as obtained through a fit of equation (1), as calculated using equation (2) and through equation (3). For waveguides, this is problematic, because both eq. (1) and (3) cannot be used due to strong artifacts as explained before.
- Pump power dependence of $I_{\text{VSL}}(l, \lambda_0)$ should show threshold behavior, i.e. a (sub)linear increase in ASE intensity, followed by a sudden shift to superlinear increase. However, when measuring power dependence, data can only be compared if acquired under similar conditions and with the same experimental settings.

3 Experimental approach

In this section, we will explain in detail the experimental setups we used and the approach taken during the experiment. First we will discuss the PL experiments on samples 1401s1 and 1402s2, followed by a detailed description of the methods employed to find optical gain in all the samples.

3.1 Photoluminescence experiments

3.1.1 Experimental setup

In our first series of experiments, we investigated both the excitation power dependence and the time dependence of the PL from samples 1401s1 and 1402s2. The experimental setup we built for

this purpose is illustrated in Figure 3.1. To excite the samples, we used the third harmonic output of a standard Nd:YAG laser. The laser was set to pump at 7.2 J—well below its optimal output power—to avoid burning the samples (and our power sensors). This resulted in a less-than-stable beam that was nonetheless adequate for our purposes. To control the beam power that reached the sample, an attenuator (Glan Thompson) prism was placed directly in the path of the beam. After emerging from the GT prism, the beam then passed through a 60° splitter prism separating its two components. The splitter was angled such that only the 355 nm component passed through the diaphragm that was placed directly behind it. We used this component because it is very close to the optimal excitation wavelength of 365 nm (as determined in [4]) for these samples.

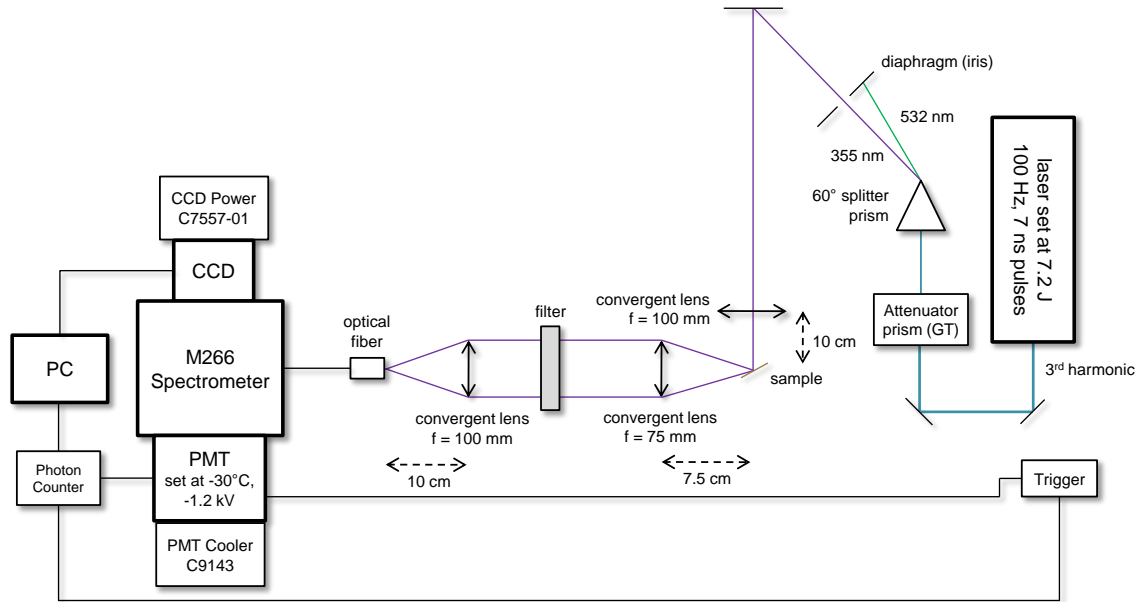


Figure 3.1: Experimental setup used to investigate the power and time dependence of the photo-luminescence from the first two samples.

After splitting, the beam was passed through a lens to focus it on the sample, which was placed in the focal point behind the lens at a 45° angle. The emitted light was then passed through more lenses, as well as a filter (type BC8) to reduce reflections from the laser. As explained in the previous section, we would prefer our collecting lens to have a short focus in order to increase the efficiency of light collection. For this reason, we used a lens with a focal length of 75 mm, instead of the 100 mm lenses we used in the rest of the setup. An optical fiber (optimized for visible wavelengths) was used to pass the emitted light on to a spectrometer (M266), to which both a CCD and a PMT were attached. Finally, the signals from the PMT and CCD were passed on to a computer, which recorded the data, though in the case of the PMT the signal was first passed through a photon counter (Fast Comtec P7887) before reaching the PC, together with the signal from a trigger that was placed close to the laser.

3.1.2 Measuring the power dependence

Before commencing the power dependence experiment, we first performed a calibration measurement of the attenuator prism in order to relate the power of the laser beam hitting the sample to the attenuator angle. This was done by placing a joule meter in front of the sample and recording the energy of the beam at different settings of the attenuator. With the calibration completed, we then recorded PL spectra for both samples at every known attenuator setting using the CCD branch of the setup. The CCD was set to detect around 550 nm for sample 1401s1 and around 620 nm for sample 1402s2, with slit widths of 100 and 500 μm respectively. Using the calibration

data it was then possible to relate PL intensity to pumping intensity.

To correct for stray light and other noise, we also performed a so-called ‘dark’ measurement, where the laser beam was blocked temporarily. The background spectrum generated in this measurement was then subtracted from the other spectra and the resulting data was normalized for analysis. The normalization procedure corrected for different duration of the measurements at the different attenuator angles and we did not vary any other settings in between measurements on the same sample.

3.1.3 Measuring the time dependence

For this part of the experiment, we used the PMT branch of the setup. The PMT was cooled down to $-30\text{ }^{\circ}\text{C}$ and a potential difference of -1.2 kV was applied to it. For sample 1401s1 we set the detector around 518 nm (central peak wavelength as determined by previous results) with a slit width of $15\text{ }\mu\text{m}$ and a bin width of 0.25 ns . This led to a temporal detection window of 640 ns , i.e. we were able to detect how many photons were coming in at different points in time up until a maximum of 640 ns after each laser pulse.

For the second sample, we set the detector around 571 nm with a $20\text{ }\mu\text{m}$ slit and the same temporal resolution. We measured the number of incoming photons as function of time in this way for several different pumping intensities, mostly at lower power (i.e. below saturation level, as determined from the previous results) but including one or two higher powers as well. Finally, we increased the bin width to 64 ns , cranking the temporal detection window up to $164\text{ }\mu\text{s}$ in case there was some slow component not visible within the shorter time-frame of the earlier measurements. By fitting the data obtained this way with a double exponential decay function we will be able to determine the decay times and relative strengths of the different decay components.

3.2 Optical gain experiments

3.2.1 Experimental setup

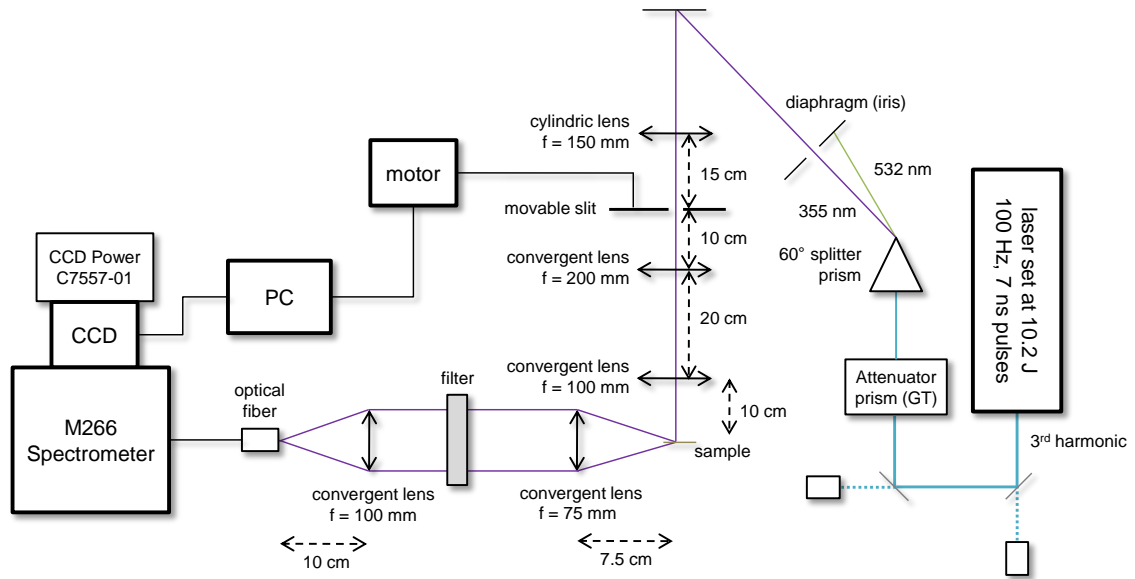


Figure 3.2: Experimental setup used to investigate optical gain in all samples, using the VSL and SES methods.

In our second series of experiments, we focused entirely on trying to find optical gain. For this purpose, we reconfigured our previous setup for VSL and SES measurements. The new setup is

illustrated in Figure 3.2. Compared to the previous setup, we added a cylindrical lens to focus the beam in the vertical direction, as well as the movable slit that is integral to both VSL and SES techniques (connected to the PC via a micro step motor). Our slit was reconfigurable by hand to serve both the purpose of the moving screen for VSL measurements as well as that of the moving slit for SES. Other changes include:

- The addition of another lens between the slit and the sample to help focus the beam and get a clean thin stripe
- Rotation of the sample so that its edge now faces the detector, in accordance with VSL prescription
- The replacement of two mirrors by quartz slides (indicated in gray in the illustration) to weaken the laser beam, which is now set to pump at 10.2 J—much closer to its optimal setting.

This last was necessary to get a stable beam with a good profile. Unfortunately, due to the strength of the beam our GT prism burned from the inside out and we had to replace it with a slightly broken one (this was before we had replaced the mirrors with quartz slides). The two quartz slides reflect only about 4% of the incident light (the rest is absorbed by strategically placed beam stoppers), so that the remaining components—including the precious samples—only have to deal with 0.16% of the original beam strength.

3.2.2 Measuring VSL and SES

As in the PL experiments, we first investigated the relation between attenuator angle and excitation beam power. In addition, because it is essential for VSL and SES to have a good laser beam profile in both spot and stripe configurations, we used a beam profile detector (SP503U) to visualize the shape of the laser beam at the sample location (i.e. after it has passed through the movable slit/screen). Using this visualization, we calibrated the motor and the movable slit in such a way that setting the motor—in VSL configuration—to location ‘zero’ would create the narrowest possible stable spot.

After finishing these calibrations, we first investigated optical gain in rhodamine 6G—a well-known gain medium—in order to test our setup. It should be said that the rhodamine sample we had on hand was not optimized for optical gain measurements. The sample in question consisted of a low-concentration liquid solution (in UV-ethanol) encased in a rectangular parallelepiped quartz cuvette.

A semi-automatic process, first developed by Kateřina Dohnalová and subsequently improved by the author, operated the motor and CCD software so that ASE spectra were recorded for variable slit lengths from 0 to 4000 μm , with a step size of 100 μm . After this process was completed, manual reconfiguration of the movable slit into SES mode was required, then the script was executed again to record ASE spectra for variable spot locations, also from 0 to 4000 μm . For these measurements, the CCD was configured to detect around 550 nm—close to the lasing range for this material—with an (internal) slit width of 22 μm . This was done for one specific excitation beam power—144 μJ , the point at which the material stopped lasing (more about that in section 4.2.1). Of course, background was again subtracted from the spectrum before processing.

Next, we investigated all the $\text{a-SiO}_x\text{N}_y$ samples in a similar way, recording the beam profile every time and calibrating the motor accordingly. For these measurements we also set the CCD to 550 nm, but with an internal slit width of 2000 μm and, in all but the first sample measurement, using a maximum stripe length of 4500 μm instead of just 4000. ASE spectra were recorded, not just for one specific excitation power, but for as many different values as possible, starting at the lowest value of 8.7 μJ and working up to the highest value of 368 μJ .

The data thus obtained was processed using a collection of algorithms and subroutines developed by the author specifically for this purpose (see Appendix A for a detailed description). This processing consisted of smoothing, reduction, integration, normalization, subtraction and plotting,

in that order. The spectral data was first smoothed to remove noise, using a window of 20 points (total points were 2060). After that, data reduction took place in order to speed up processing, reducing spectral resolution from 0.2098 nm to 3.3568 nm. Next, the SES data were integrated over the whole stripe, after which normalization through linear regression was performed on both VSL and integrated SES (intSES) data at the same time.

During linear regression, a linear fit is made through the first few data points (corresponding to the first few hundred micrometer stripe length / spot position) of both the VSL and intSES data. By subtracting the ‘a’ parameter (i.e. the y-intercept, or ‘zero intensity’ value) from both fits independently, any remaining background noise is removed. After this, the intSES data is divided by the ‘b’ value, or slope, of its own fit and multiplied by the slope of the VSL data. This is done to ensure that VSL and intSES data match for short stripe lengths—as they should, according to the theory.

As explained in section 2, SES data correction is unavoidable when dealing with an SES spot size larger than the motor step size. However, due to the nature of this correction, a small change in parameters (i.e. the number of points taken for linear regression) can have a big impact on the outcome of the whole project. Therefore, care should be taken when interpreting the results of the calculations and they should always be verified by other means in order to avoid false positives.

Finally, the normalized intSES data is subtracted from the VSL data and the difference is plotted in a contour map showing its dependence on wavelength and stripe length. In addition, when any interesting features show up at a particular wavelength, such as strong gain or induced absorption, a separate plot is made of the VSL and intSES curves at that wavelength. This is done to verify that the effect is really there and not due to some artifact, which would usually be clearly visible when looking at the two lines together. Contour maps and VSL vs. intSES curves are plotted for six different excitation powers where possible, to make it easy to discover patterns and to compare data from the different samples.

4 Results and discussion

In this section, we present our results and attempt to explain them within the (theoretical) confines of this report. We start with the basic photoluminescence properties of samples 1401s1 and 1402s2, continue on with optical gain measurements in rhodamine 6G and our samples and finally compare the influence of the different structures and compositions on the gain results.

4.1 Photoluminescence experiments

The PL spectra of samples 1401s1 and 1402s2 are plotted together in Figure 4.1, for both high (1.26 mJ) and low (8.6 μ J) excitation power. In this plot we can see that the PL spectrum of the first sample is centered around 518 nm, while the spectrum of the second sample is centered around 605 nm. Any visible structure is most likely caused by interference on the thin layer. This explanation is supported by the fact that the dominant peak in the spectrum of the second sample is different for different powers, while at the same time the spectrum as a whole is slightly shifted. If the spectrum in reality has a Gaussian shape and the peaks are indeed caused by interference, then we would indeed expect a shift in the interference pattern (i.e. a shift in the dominant peak) with a shift of the center of the Gaussian curve.

Figure 4.1 shows that the center of the curves (ignoring the structure) corresponds to predominantly green emission from the first sample, while the second sample has predominantly orange emission. Apparently, a higher concentration of silicon causes a red-shift of the center, so the emission is tunable by varying the composition. This is consistent with earlier results by Huang et al. on similar samples, who attribute the PL to a combination of radiative recombination in the localized states related to Si–O bonds and *a*-Si nanoparticles present in the Si-rich sample [6]. Finally we can see that the emission from these samples is quite spectrally broad, covering the whole visible range and beyond—a clear confirmation that we are dealing with an amorphous material, as expected.

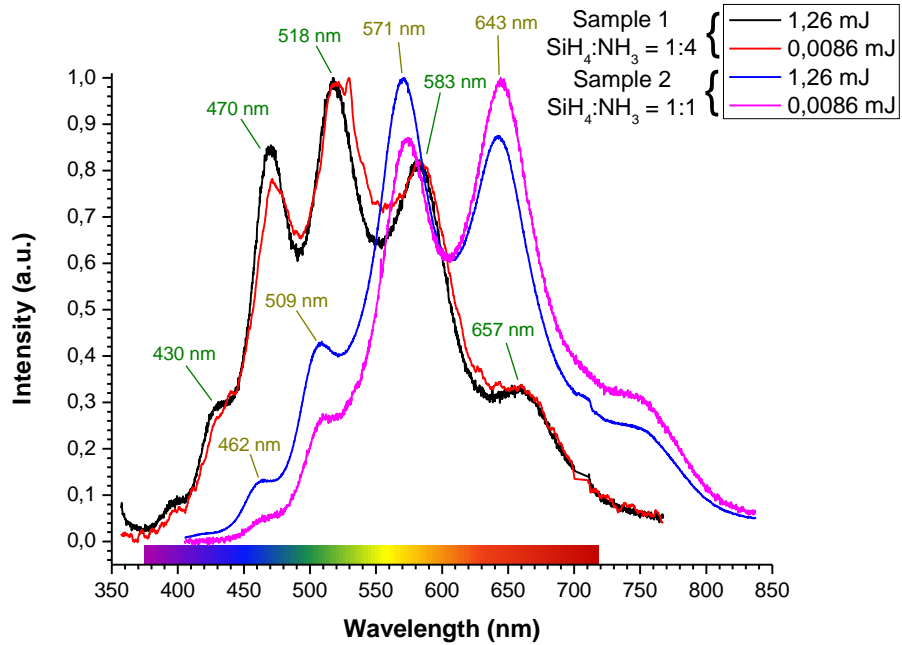


Figure 4.1: PL spectra of samples 1401s1 (sample 1) and 1402s2 (sample 2) at both highest and lowest excitation power. One of the spectra (red line) has been smoothed for better comparison.

4.1.1 Power dependence

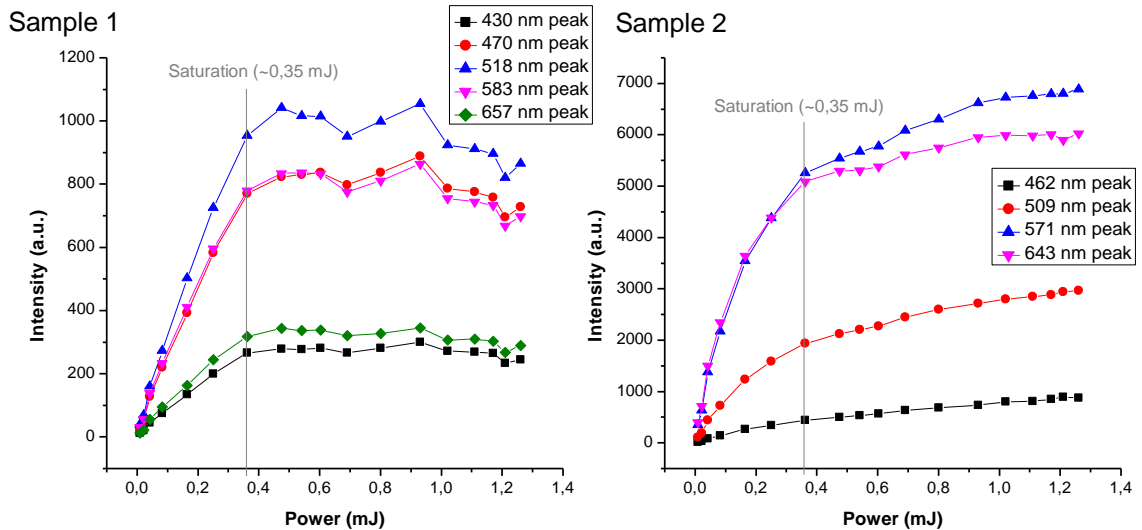


Figure 4.2: Dependence of different PL peak intensities on excitation power for both samples 1401s1 and 1402s2. The excitation power at which saturation started is indicated in gray.

Figure 4.2 shows the power dependence of the PL intensities of the different peaks in the spectrum. Samples 1401s1 (N-rich) and 1402s2 (Si-rich) are shown in separate plots, the former on the left and the latter on the right. There are a number of conclusions we can draw from these plots. First of all; since all peaks have a similar dependence, they probably have the same origin as well, which supports the earlier statement that they were caused by interference.

Second; both samples show saturation behavior above ± 0.35 mJ, but the first sample shows

a clear saturation point (and even starts to burn in the end, reducing PL intensity), while the second sample was not fully saturated (PL keeps increasing with increasing stimulation) even at the highest power. This difference in saturation behavior might be due to the presence of Si nanoparticles in the Si-rich sample. However, since we have not done any TEM measurements, we cannot be sure that there were nanoparticles present in our sample, so this is pure speculation. The fact that there is saturation behavior at all, though, can be attributed to the defect-origin of the luminescence (e.g. luminescent centers related to Si-O bonds, as suggested in [4]).

4.1.2 Time dependence

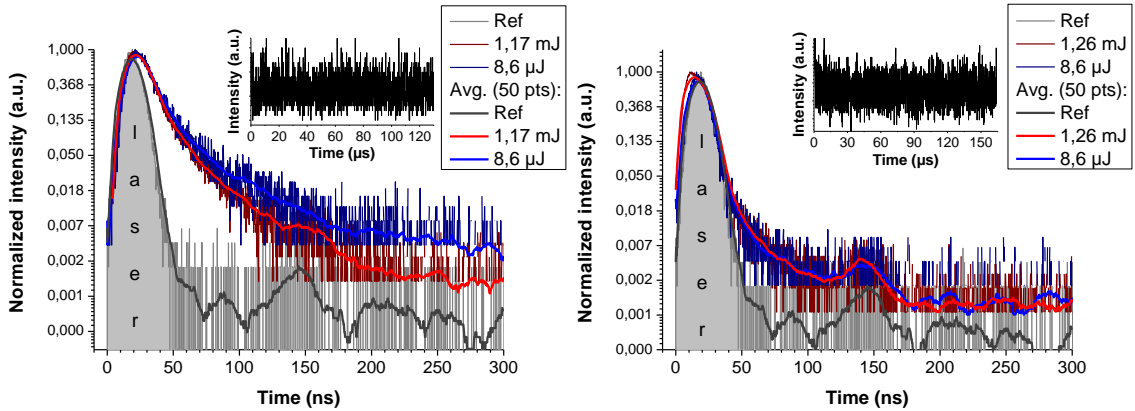


Figure 4.3: Time dependence of the PL for both samples 1401s1 (left) and 1402s2 (right) for high and low excitation power. The shape of the laser and electronic response is shaded gray (Ref line). Extra smoothed lines have been added for better comparison. The inset shows the PL response on a larger time-scale.

In Figure 4.3 the decay of the PL response in time has been plotted for the samples 1401s1 (left) and 1402s2 (right). Like with the power-dependence plots, we have again taken only the highest and lowest excitation densities and left the rest out of the picture. Extra smoothed lines have been added to the plots to make it easier to compare the trends. To eliminate laser pulse and system response delay from the data, we also took a measurement at the excitation wavelength of 355 nm (shaded gray area marked ‘laser’ and ‘Ref’ lines).

In the plot for sample 1401s1, we can clearly distinguish two fast decay components. Note: since the high power response has been measured at a different time for the first sample, under slightly different experimental conditions, there is a slight difference between the low and high power decays. In the other plot, there are also two fast components, but one of them is clearly very weak (witness the fact that the PL response seems to be ‘hugging’ the shaded gray area). From the insets, we know that there are no slow (i.e. in the order of a few μ s) components in either of the two samples. We assume the temporary increase in PL around 150 ns to be due to an artifact. There is no discernible difference between the decay at low and high pumping power (aside from the aforementioned difference due to changed experimental conditions).

The relatively large (time-wise) laser profile and electronic response of this setup effectively obscures the quickly decaying PL response in these samples, making it very hard to obtain an accurate fit of the data. All attempts at automatic deconvolution of the laser signal from the data have failed. Our best attempt at manual deconvolution and fitting of a double exponential decay curve to the data has led to the following results; for the first sample, the fitted decay constants for the highest excitation power were found to be: $\tau_1 \simeq 8.5(8)$ ns and $\tau_2 \simeq 34(5)$ ns. For the second sample, the fitted decay constants for the highest excitation power were found to be: $\tau_1 \simeq 3(3)$ ns and $\tau_2 \simeq 25(8)$ ns.

Later, the PL decay in these samples was also investigated using a fast picosecond laser (laser

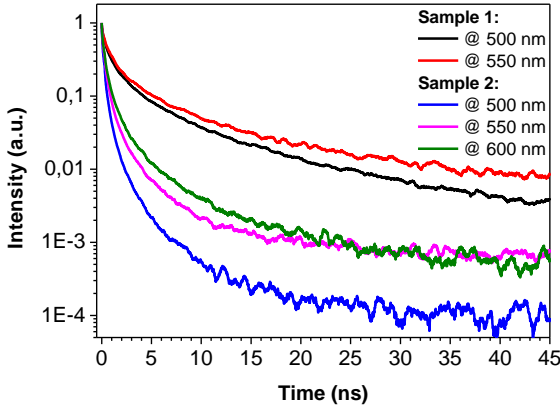


Figure 4.4: Time dependence of the PL at several different wavelengths for both samples 1401s1 and 1402s2 on a short time-scale. Data was smoothed.

pulse width ~ 20 ps), which excited the samples at 370 nm. Several different emission wavelengths were investigated; 500 nm and 550 nm for sample 1401s1, and 500 nm, 550 nm and 600 nm for sample 1402s2. The results are plotted in Figure 4.4. The influence of additional nitrogen (sample 1) is clearly visible in these preliminary results, as it was in the earlier measurements; it results in slower decay in all cases. This is most likely caused by passivation of trapping states by N. In the Si-rich sample, these trapping states cause ultra-fast quenching of the PL.

For the first sample, we were able to fit the data directly with a stretched exponential decay model: $I = \exp(-(t/\tau)^\beta)$. This model is characteristic for a disordered system, with a distribution of decays for a single emitting source. Data from the second sample could not be fitted without deconvolution, because of the fast decay of the PL. For both sets of data convolution of the signal with the laser pulse was an issue, but for sample 1402s2, which had a much faster decay, it was a much greater issue. As a rough estimate, then, the parameters obtained in the fit for the first sample will be listed here; at 500 nm the fit resulted in $\tau = 0.502(16)$ ns and $\beta = 0.396(6)$, while at 550 nm it gave us $\tau = 0.623(18)$ ns and $\beta = 0.392(5)$. Please note, though, that in order to obtain accurate values, deconvolution is still required, even for the first sample.

4.2 Optical gain experiments

In this section, results from the optical gain experiments will be discussed. We will start with rhodamine 6G and then move on down the list of samples in the order of table 1.

4.2.1 Rhodamine 6G

When investigating this material, we tried out different excitation powers and found that our sample actually started lasing when the beam power exceeded ~ 144 mJ. The lasing effect was, however, most likely increased by the shape of the cuvette, which acted as a laser cavity. Still, this behavior can be taken as proof that light amplification was present in this system.

The laser spot (i.e. ‘zero’ slit width) profile, displayed in Fig. 4.5, was estimated to be about 90 μm FWHM. This was about the narrowest that we could make it without the diffraction pattern—caused by Fresnel diffraction on the slit—ruining the profile. With the slit fully opened to 4 mm, the laser stripe profile showed similar diffraction at the start and end (length-wise) of the stripe.

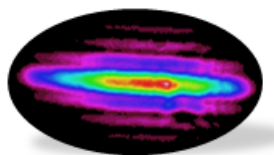


Figure 4.5: Laser spot profile during measurements on the rhodamine 6G sample.

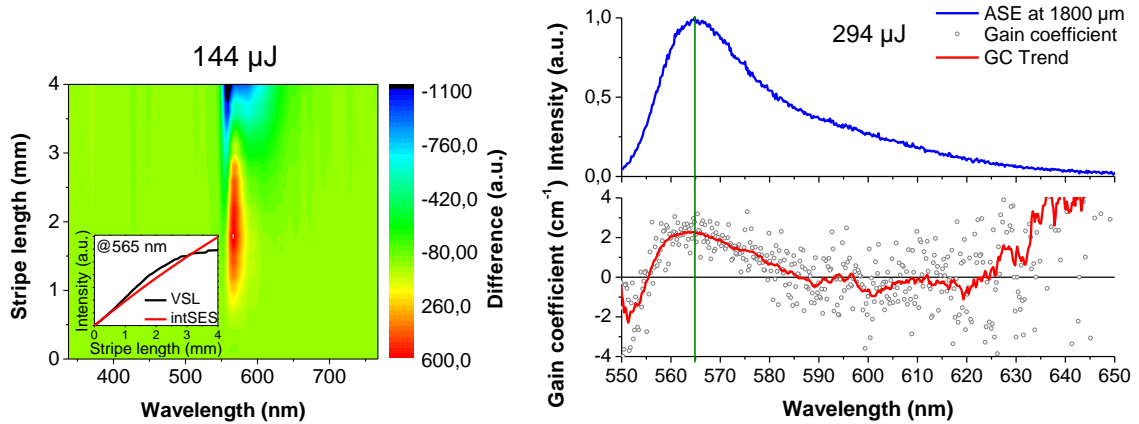


Figure 4.6: *Left:* Contour map of the differences in ASE intensity between VSL and integrated SES (intSES) data for 144 μJ beam power. The inset shows VSL and intSES curves at 565 nm plotted together against stripe length. *Upper right:* Normalized ASE spectrum at 1.8 mm stripe length recorded with a beam power of 294 μJ . *Lower right:* Calculated gain coefficient at an excitation intensity of 294 μJ .

Figure 4.6 (left) shows a contour plot of the differences between ASE intensity obtained through the VSL method and the integrated ASE intensity obtained through the SES method at 144 μJ excitation beam power, generated according to the procedure outlined in section 3.2.2. We can clearly see the optical gain in this plot in the form of a big red spot in the center. It seems to be concentrated in a narrow spectral region around 565 nm wavelength, starting at 1 mm stripe length and saturating at 3 mm. The inset shows the same story again for the central gain wavelength; for small stripe lengths the VSL and intSES data overlap, then the VSL data increase more strongly than the intSES data, indicating gain, to finally drop below the intSES data again at the saturation stripe length.

Figure 4.6 (right) shows the ASE intensity at 294 μJ excitation beam power, with a peak around 565 nm—the same wavelength as where the gain showed up before, although at this energy the sample was already lasing. This result shows that our setup is working as expected, but to verify we also calculated the net gain as a function of ASE wavelength using eq. (2) with stripe length $l = 900 \mu\text{m}$. The result of this calculation is plotted in the lower graph of Figure 4.6 (right), and shows positive gain in the region 555 nm to about 585 nm, with a maximum of $2.2(4) \text{ cm}^{-1}$. Note: the increase in the gain coefficient at wavelengths greater than 620 nm is assumed to be an artifact, as the ASE intensity becomes too low for accurate calculation.

Figure 4.7 shows the ASE spectra at 0 and 4 mm stripe length for a beam power of 294 μJ . Because the ASE spectra apparently are a convolution of two Gaussian functions, we fitted these spectra with a double Gaussian peak (red lines in figure). This allowed us to obtain the peak widths at half-maximum for each individual peak in the spectra. Using these values, we could calculate the gain coefficient through equation (3). To do this, we plugged in the peak width at 0 mm stripe length as $\Delta\nu_0$, and the peak width at 4 mm stripe length as $\Delta\nu_{\text{ASE}}$, and used a computer to solve for G . For the first peak (green lines in Fig. 4.7) this resulted in a value of $2.3(4) \text{ cm}^{-1}$, which appears to be consistent with the earlier result. For the second peak, we found that $G \simeq 1.6(4) \text{ cm}^{-1}$, which is still consistent with the earlier result within the error margins.

As a last check, we fitted the VSL data with eq. (1), obtaining a value of $5.4(6) \text{ cm}^{-1}$ at 294 μJ excitation power. This is more than double the previous values, so it is likely that part of it is due to artifacts such as e.g. the confocal effect. If the earlier results were correct, than this would indicate that this method of calculating optical gain is indeed very inaccurate.

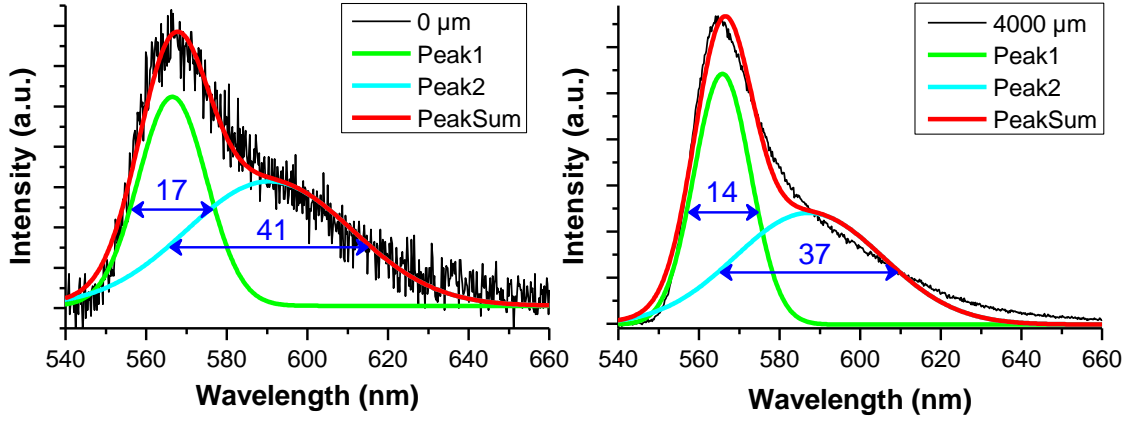


Figure 4.7: ASE spectra at $294 \mu\text{J}$ for 0 and $4000 \mu\text{m}$ stripe lengths (black). The red lines represent double Gaussian peak fits, with the separate peaks plotted in green and cyan. The values indicated in blue are FWHM values as determined by the fits.

4.2.2 Sample 1401s1

Note: for this sample, we forgot to re-calibrate the motor and record the beam profile. However, since we did not change any part of the setup in between measurements, we will assume it did not change.

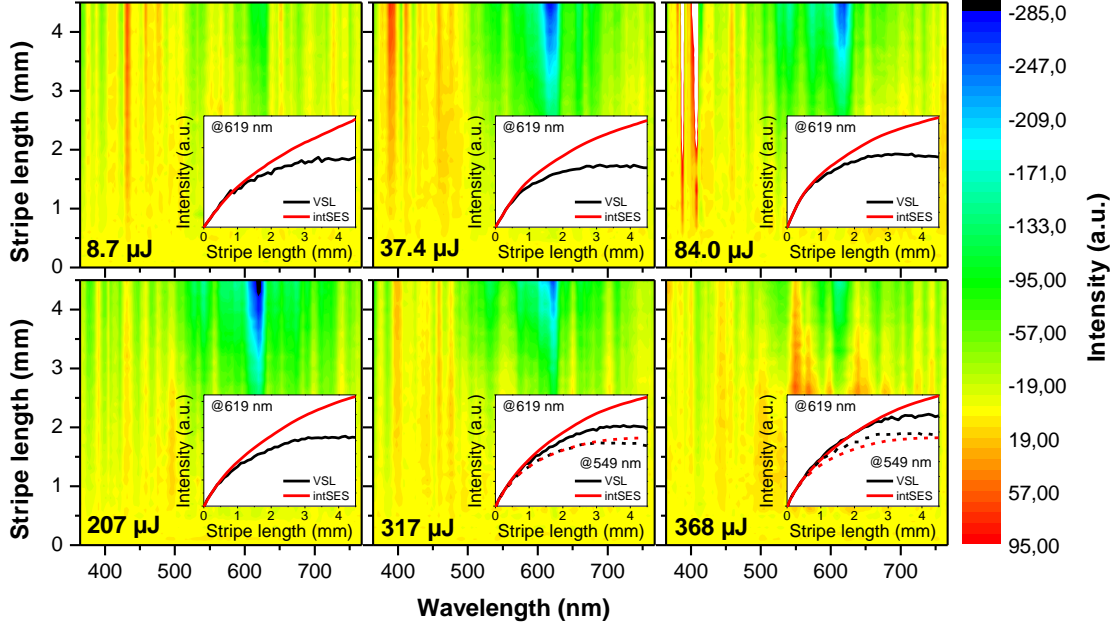


Figure 4.8: Contour maps of the VSL and integrated SES (intSES) differences plotted for different excitation power against wavelength and stripe length. The insets show the separate VSL and integrated SES curves at 619 nm . For the two highest powers, the insets also show VSL and intSES curves at 549 nm (dashed lines).

Figure 4.8 shows the generated contour maps outlining the $\text{VSL}-\text{intSES}$ difference for different excitation powers. There appears to be some induced absorption around 619 nm , which is present at all powers but gradually lessens when the beam power gets very high (a sign that the gain is increasing faster than the losses). The ‘red stripes’ visible around $400-500 \text{ nm}$, as well as

those > 700 nm, are believed to be due to laser reflections and other artifacts—such as too much background subtracted from the SES data—and not actual gain. These are generally very spectrally narrow, while we expect any gain to be relatively broad, like the induced absorption that is visible here.

At the highest excitation power— $368 \mu\text{J}$ —there appears to be gain around 549 nm, very similar to what we saw in rhodamine 6G (see also dashed lines in inset), which was not present at $317 \mu\text{J}$. To verify this, we plotted the net gain obtained through equation (2) using $l = 1000 \mu\text{m}$ stripe length, just like we did for our rhodamine sample. The results were not encouraging—we got only negative coefficients in the whole spectral region 500 – 600 nm, with $G(549) \simeq -18 \text{ cm}^{-1}$. Furthermore, a plot of the power dependence did now show any threshold behavior. Thus we can conclude that the apparent gain we found by comparing VSL and intSES data was most likely caused by burning of the sample or other artifacts (such as waveguiding effects).

4.2.3 Sample 1402s2

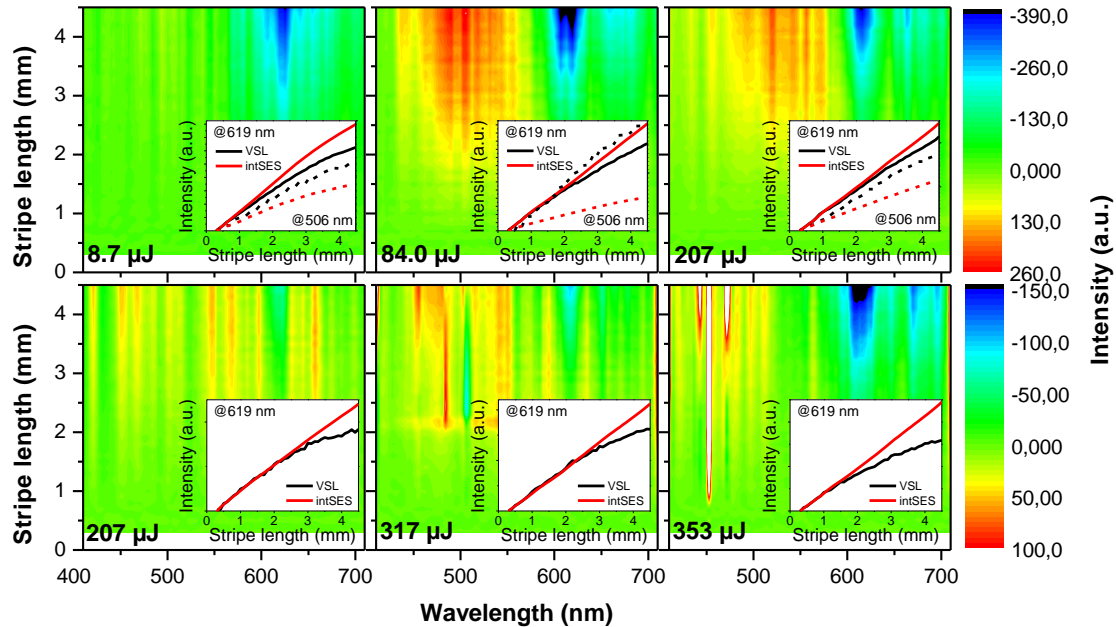


Figure 4.9: Contour maps of the VSL and integrated SES (intSES) differences plotted for different excitation power against wavelength and stripe length. The insets show the separate VSL and integrated SES curves at 619 nm. For the lower powers, the insets also show VSL and intSES curves at 506 nm (dashed lines). Note: a new place on the sample was selected for each plot on the bottom row, and the measuring time was much shorter than for the top row.

Figure 4.9 shows the generated contour maps outlining the VSL–intSES difference for different excitation powers. Due to severe burning of the sample at higher power (leaving visible, sand-colored marks even at half power), we had to measure the higher powers independently, each at a different location on the sample and with shorter measuring times. The data thus obtained is represented by the bottom row of plots. Note: there are two plots for $207 \mu\text{J}$, because we felt it prudent to retake the last measurement in the sequence 8.7 – $207 \mu\text{J}$ at a new location on the sample, with different settings.

There appears to be some induced absorption around 619 nm in this sample, just like in sample 1401s1, which seems to keep increasing with higher power (though it is hard to tell, because the top and bottom rows of the figure cannot accurately be compared). The slight decrease at $207 \mu\text{J}$, top row, is most likely because the sample was already burning by then.

Aside from the induced absorption, there also appears to be significant gain around 506 nm, especially at 84 μ J—remarkable, considering the level of excitation at that point. However, this apparent gain could very well be due to a fitting artifact; when examined closely, it can be seen that the VSL curve (dashed black lines in the insets) behaves very differently during the first 600–700 μ m of the measurement. This behavior could be caused, for example, by loose screws on our slit. The data presented in Fig. 4.9 have already been cut to produce cleaner results: the first 300 μ m were removed (white space in the contour plots). However, this might have been insufficient by itself to completely correct for this artifact. To eliminate artifacts as the cause of the gain, we plotted the power dependence of the ASE around 506 nm, and calculated the gain through equation (2) using $l = 2000 \mu\text{m}$.

The power dependence graph (Fig. 4.10) clearly shows that the sample is burning, as there is a sharp decline in ASE intensity starting from 84 μ J. Before that, the double logarithmic slope is sub-linear (~ 0.5), with no threshold behavior visible. The gain coefficients we calculated for the three lowest powers in Fig. 4.9 (top row), -3 for 8.7 μ J, -18 for 84 μ J and -5 for 207 μ J, were all negative and so confirmed our suspicion that the apparent gain around 506 nm was due entirely to an artifact.

Moving on to the higher power plots, the bottom row of Fig. 4.9, we see a lot of ‘red stripes’ again. These can also be attributed to artifacts, which were increased by the fact that the measuring time was much shorter, leaving more room for error because of the weaker signal. Thus we can conclude that on this sample, as on the first, there is no true gain to be found either.

4.2.4 Sample 1369s2

We were unable to measure anything on this sample, because the luminescence was fading visibly even at low power, indicating that the sample was burning very quickly. Apparently there was very strong absorption in this particular sample.

4.2.5 Sample 1369s4

Figure 4.11 shows the generated contour maps outlining the VSL–intSES difference for different excitation powers. This sample appears particularly promising, because in addition to strong induced absorption, we can see three separate instances of possible gain:

- At the lowest powers (top row) there appears to be some gain around 441 nm.
- At 266 μ J there appears to be gain around 589 nm for stripe lengths between 400 and 1600 μ m, which then saturates. This looks very similar to what we saw for our rhodamine sample.
- At 368 μ J there appears to be very strong gain in a broad spectral region centered around 589 nm.

Let us first discuss the shape of the VSL and intSES curves, which is different in the top and bottom rows. This could indicate that something happened to the sample in between measurements at or below 144 μ J, and at 266 μ J and above. In particular, both curves show a distinct bend around 500 μ m starting from the bottom row, which could indicate that the spot illuminated by the laser on our sample changed places in between measurements at lower and higher powers. This could happen when the sample itself, or one of the mirrors, shifted slightly during the experiment. To learn more, we plotted the power dependence in Fig. 4.12 for the two interesting wavelengths 441 nm and 589 nm. The measurement at highest excitation power cannot really be compared in

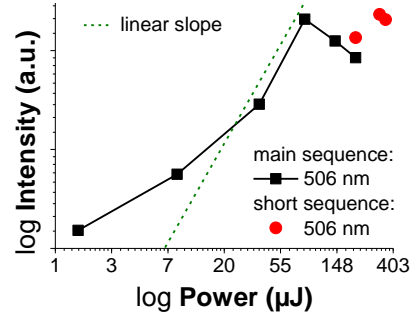


Figure 4.10: Power dependence of the ASE at 506 nm for both sequences. The dashed line provides an indication of what a linear slope would look like at this scale.

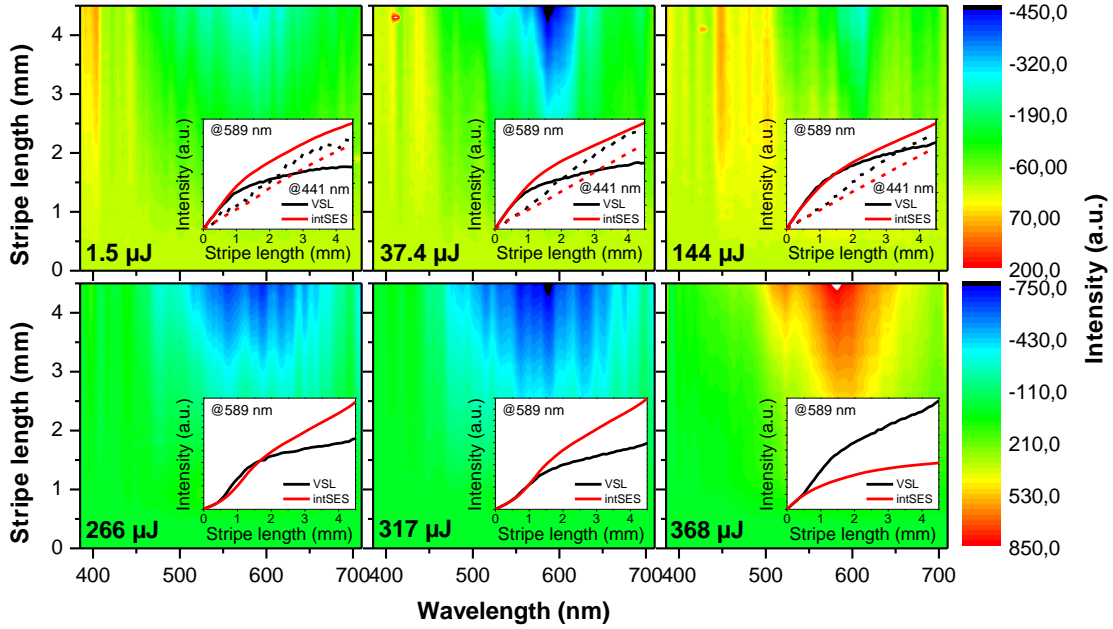


Figure 4.11: Contour maps of the VSL and integrated SES (intSES) differences plotted for different excitation power against wavelength and stripe length. The insets show the separate VSL and integrated SES curves at 589 nm. For the lower powers, the insets also show VSL and intSES curves at 441 nm (dashed lines). Note: the highest power was measured on a different day (so the sample may have shifted in between).

this way, because that measurement took place at a different date, and likely at a new location on the sample. Nevertheless, it is included in Fig. 4.12, though not connected to the main sequence.

The power dependence plot shows the expected saturation behavior, but it also confirms our suspicion that something changed during or after the measurement at 207 μJ (not included in Fig. 4.11), as there is a sudden sharp drop in ASE intensity after that. There is, however, no threshold behavior visible. The measurements at higher power (with the exception of the one at 368 μJ , for reasons explained before) show a constant level of intensity, indicating saturation, but not burning. This in spite of the fact that we have measured strong induced absorption at these powers. Apparently, this waveguide structure is good at transporting excess energy away from the source of excitation.

Moving on to the first possible instance of gain, around 441 nm at the lower powers (see also the dashed lines in the insets of the top row of Fig. 4.11). To determine whether or not this is true gain, we followed the usual procedure and calculated the net gain using equation (2) with $l = 1500 \mu\text{m}$. We found negative values around 441 nm ranging from -5 cm^{-1} for 144 μJ to -3 cm^{-1} for 1.5 μJ beam excitation power. Thus we can conclude that this instance at least is again caused by artifacts similar to the ones responsible for the ‘red stripes’ in the samples discussed before.

For the second instance, we also calculated the gain coefficient, this time using $l = 600 \mu\text{m}$. The results were surprising (in view of the previous ones); for both the 266 μJ (plotted in Fig. 4.13) and the 317 mJ measurements, we got positive results around 589 nm (as well as higher wavelengths).

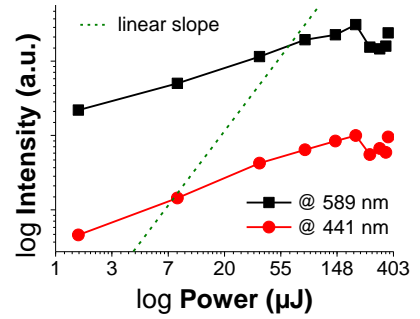


Figure 4.12: Power dependence of the ASE at 589 nm and at 441 nm. The dashed line provides an indication of what a linear slope would look like at this scale.

At 266 μJ , we found $G(589) \simeq 6 \text{ cm}^{-1}$, while at 317 μJ , we obtained $G(589) \simeq 2 \text{ cm}^{-1}$. The gain disappeared at 353 μJ , where we got $G(589) \simeq -1 \text{ cm}^{-1}$. The highest value we obtained was $\sim 10 \text{ cm}^{-1}$ around 690 nm.

The third and final instance of gain, on the other hand, turned out to be caused by artifacts again, most likely due to burning of the sample, although it is hard to tell because of the different experimental conditions under which this particular measurement was performed. Calculation of the gain coefficient using $l = 2000 \mu\text{m}$ resulted in negative values for the whole spectral region, with $G(589) \simeq -5 \text{ cm}^{-1}$. This was also the case for $l = 600 \mu\text{m}$ and for $l = 1000 \mu\text{m}$.

In conclusion, there appears to be net optical gain in a broad spectral region for 266 μJ and 317 μJ excitation beam powers. However, since a plot of the power dependence did not show the expected threshold behavior, additional measurements are required to exclude waveguiding effects as the source of this gain.

4.2.6 Sample 1374s2

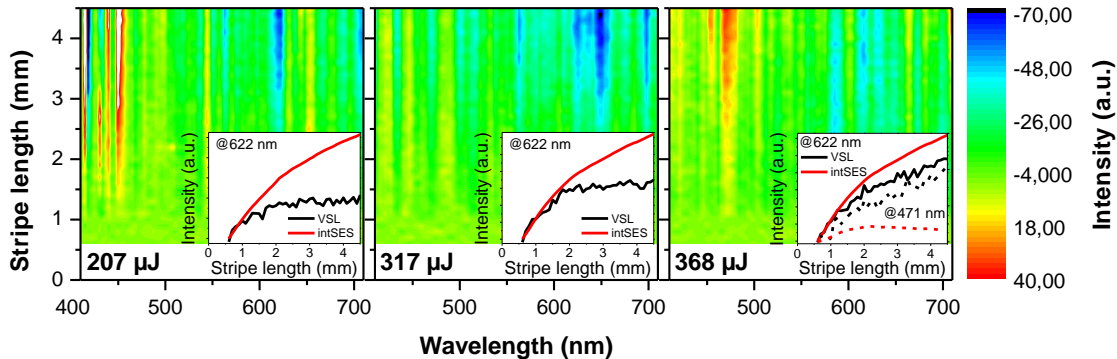


Figure 4.14: Contour maps of the VSL and integrated SES (intSES) differences plotted for different excitation power against wavelength and stripe length. The insets show the separate VSL and integrated SES curves at 622 nm, as well as at 471 nm for the highest power (dashed lines).

Figure 4.14 shows the—by now familiar—contour maps outlining VSL-intSES differences. The luminescence of this particular sample was very poor, so that we were only able to measure anything at the highest excitation powers. Even so, the differences in intensity between VSL and intSES data were very small compared to those observed in the other samples. Because of this, experimental noise had a big influence on the data and we had to cut the first 600 μJ because the amount of noise compared to useful data was so great for small stripe lengths that it ruined our calculations.

Because of the weak signal, small differences in intensity will stand out, making it hard to tell whether we are dealing with an actual observation or just an artifact. Despite this, we can clearly see some induced absorption around 622 nm. The VSL curves around this wavelength clearly show saturation, since the ASE intensity does not increase much with increasing stripe length after the first 2 mm, while the intSES curve continues to increase. The exception is the highest power, where we can see the VSL curve increasing even after 2 mm stripe length. This is most likely due to burning of the sample changing the chemical composition, allowing the ASE intensity to increase further, although the overall trend of decreasing induced absorption suggests

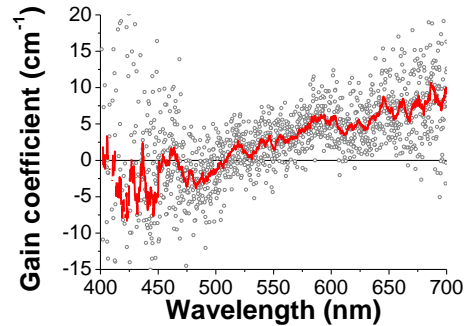


Figure 4.13: Gain coefficient calculated using eq. (2) with $l = 600 \mu\text{m}$ for 266 μJ beam power.

that it might be a case of gain increasing faster than losses (yet not enough to actually show light amplification).

Additionally, there appears to be some gain around 471 nm for the highest power, but because of the weakness of the signal and because the intSES curve quickly levels off and even starts to decrease a little at longer stripe lengths, we can almost certainly attribute this to artifacts caused by burning of the sample. The ‘red stripes’ between 400 and 500 nm at 207 μJ are also clearly due to artifacts. To be absolutely certain, we calculated the net gain coefficient around 471 nm for the highest power, using $l = 1500 \mu\text{m}$. As expected, we obtained negative values, with $G(471) \simeq -10 \text{ cm}^{-1}$. Thus we can conclude that on this sample, there is no light amplification anywhere for the powers we were able to measure.

4.2.7 Sample 1374s4

Note: for this sample, we forgot to re-calibrate the motor and record the beam profile. However, since we did not change any part of the setup in between measurements, we will assume it did not change. Also, this sample had visible stress around the edges (i.e. we could *see* a difference in structure between the edge of the sample and the interior). This stress will probably have distorted the layer, causing some major discrepancy in the data between short and long stripe lengths.

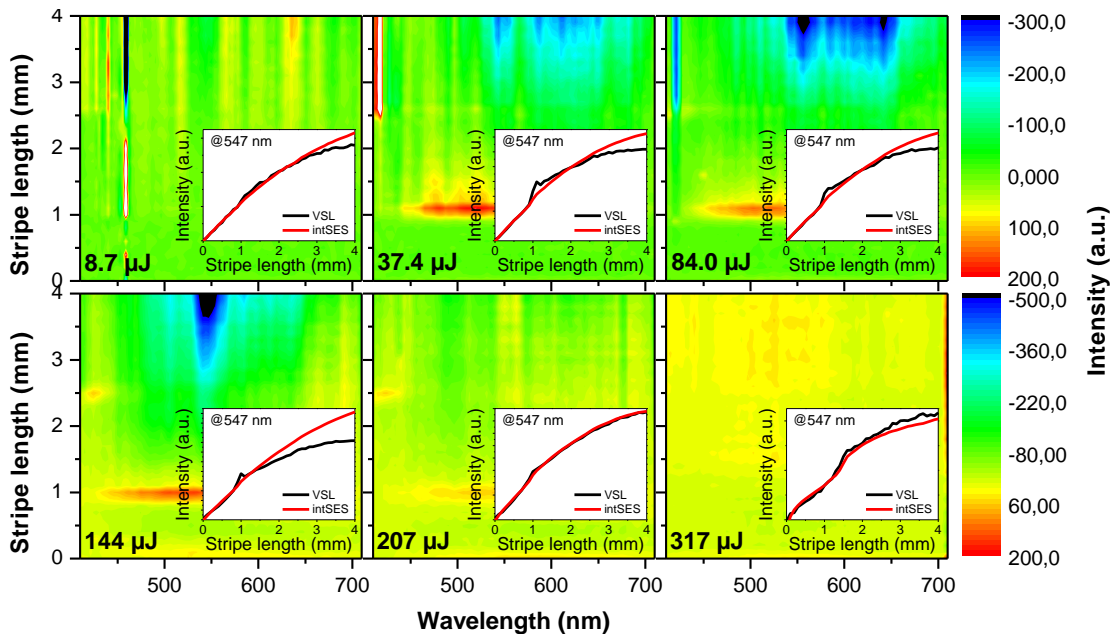


Figure 4.15: Contour maps of the VSL and integrated SES (intSES) differences plotted for different excitation power against wavelength and stripe length. The insets show the separate VSL and integrated SES curves at 576 nm. Note: top and bottom rows were measured on different days.

Figure 4.15 does indeed show a discrepancy in the data, in the form of a ‘bump’ in the VSL data at 1 mm stripe length. This is also visible as an elongated red spot in the contour plots. Due to this artifact, it is hard to interpret the data correctly. To correct for this, we took more points for linear regression while normalizing the data for this sample; 10 for the lower powers (top row in Fig. 4.15) and 15 for the higher powers, where the effect of the distortion was stronger (bottom row). Due to this stronger correction, it is however possible that any gain that might have been present is no longer visible.

In any case, we can see some induced absorption around 576 nm, which first gets stronger and then disappears when we go to higher excitation powers (again, this might be because the gain is

winning out over the losses, as in the previous sample). There is however no positive difference between VSL and integrated SES visible. Calculation of the net gain coefficient using equation (2) with $l = 1500 \mu\text{m}$ confirmed that even at $317 \mu\text{J}$ there was no net gain ($G(547) \simeq -8 \text{ cm}^{-1}$). However, due to the bad quality of the sample these results should not be taken as absolute proof. To affirm our conclusion of no net gain, a better sample would be needed.

5 Conclusion

The PL spectra we obtained are similar to earlier results and support the conclusion that the PL is tunable by varying the amount of nitrogen and silicon with which the samples are created. Furthermore, when comparing the influence of the composition on the PL properties (section 4.1), it was clear from the power dependence measurements that the presence of extra nitrogen led to slower decay times and to strong saturation behavior. However, because of that (as we saw in section 4.2) the N-rich samples were more resistant to burning than the Si-rich ones. The origin of these differences is thought to lie with the Si–O bonds, which can act as luminescent centers, providing the system with additional (defect-like) states.

The influence of the waveguide structure was immediately visible in that we had a hard time measuring anything on samples 1369s2 and 1374s2, which both have waveguide structure (a). The combination with more nitrogen (1369s2) was particularly bad in terms of optical properties. Where we did measure something (1374s2), we did not find any evidence of net optical gain, although the results were not very clear due to the weakness of the signal.

In contrast, waveguide structure (b) appears much more suitable for optical applications, providing a nice strong signal for both samples 1369s4 (N-rich) and 1374s4 (Si-rich). In the first case we even found net optical gain for two different excitation intensities; at $266 \mu\text{J}$, we found $G(589) \simeq 6 \text{ cm}^{-1}$ and at $317 \mu\text{J}$, we obtained $G(589) \simeq 2 \text{ cm}^{-1}$. However, additional research is needed to verify this result and to exclude waveguiding effects as the source of this gain. In the case of sample 1374s4, we did not find any positive gain but the results are inconclusive due to the bad quality of the sample.

In the case of the 2D planer waveguide samples 1401s1 and 1402s2, we did not find any clear evidence of net optical gain. To clear up the data, it would be advisable for future measurements to reverse the order of VSL and SES measurements (i.e. to start with SES measurements, which are less taxing on the sample, and only then conduct VSL measurements). This can exclude any apparent gain caused by a changed chemical composition due to burning of the sample while reducing the need for manual correction.

Finally, to confirm the presence (or lack of) actual light amplification, it is advisable to re-measure at least some of the samples using versions of higher quality than the ones used in this experiment. In particular, the two samples with waveguide structure (b) should be re-examined. If the presence of net optical gain in sample 1369s4 can be confirmed by a second measurement, then this would be a big step forward in the development of a Si-based laser.

Acknowledgments

I would like to thank my supervisor, Kateřina Dohnalová, for her invaluable assistance during the project, and Kunji Chen from the Department of Physics, National Laboratory of Solid State Microstructures, Nanjing University in China for providing the samples that were used in the experiments.

References

- [1] L. Pavesi. Silicon-Based Light Sources for Silicon Integrated Circuits. *Advances in Optical Technologies*, 2008, 2008. [doi:10.1155/2008/416926](https://doi.org/10.1155/2008/416926).
- [2] David J. Lockwood. Light emission in silicon nanostructures. *Journal of Materials Science: Materials in Electronics*, 20(1):235–244, 2009. [doi:10.1007/s10854-007-9552-6](https://doi.org/10.1007/s10854-007-9552-6).
- [3] L. Pavesi, L. Dal Negro, D. Mazoleni, G. Franzo, and F. Priolo. Optical gain in silicon nanocrystals. *Nature*, 408(6811):440–444, 2000.
- [4] Rui Huang, Kunji Chen, Bo Qian, San Chen, Wei Li, Jun Xu, Zhongyuan Ma, and Xinfan Huang. Oxygen induced strong green light emission from low-temperature grown amorphous silicon nitride films. *Applied Physics Letters*, 89(221120), 2006. [doi:10.1063/1.2399393](https://doi.org/10.1063/1.2399393).
- [5] Rui Huang, Kunji Chen, Peigao Han, Hengping Dong, Xiang Wang, Deyuan Chen, Wei Li, Jun Xu, Zhongyuan Ma, and Xinfan Huang. Strong green-yellow electroluminescence from oxidized amorphous silicon. *Applied Physics Letters*, 90(093515), 2007. [doi:10.1063/1.2711196](https://doi.org/10.1063/1.2711196).
- [6] Rui Huang, Kunji Chen, Hengping Dong, Danqing Wang, Honglin Ding, Wei Li, Jun Xu, Zhongyuan Ma, and Ling Xu. Enhanced electroluminescence efficiency of oxidized amorphous silicon nitride light-emitting devices by modulating Si/N ratio. *Applied Physics Letters*, 91(111104), 2007. [doi:10.1063/1.2783271](https://doi.org/10.1063/1.2783271).
- [7] Hui Chen, Jung H. Shin, Philippe M. Fauchet, Joo-Yeon Sung, Jae-Heon Shin, and Gun Yong Sung. Ultrafast photoluminescence dynamics of nitride-passivated silicon nanocrystals using the variable stripe length technique. *Applied Physics Letters*, 91(173121), 2007. [doi:10.1063/1.2803071](https://doi.org/10.1063/1.2803071).
- [8] V. A. Belyakov, V. A. Burdov, R. Lockwood, and A. Meldrum. Silicon Nanocrystals: Fundamental Theory and Implications for Stimulated Emission. *Advances in Optical Technologies*, 2008, 2008. [doi:10.1155/2008/279502](https://doi.org/10.1155/2008/279502).
- [9] Amir Sa'ar. Photoluminescence from silicon nanostructures: The mutual role of quantum confinement and surface chemistry. *Journal of Nanophotonics*, 3(032501), March 2009. [doi:10.1117/1.3111826](https://doi.org/10.1117/1.3111826).
- [10] Kateřina Dohnalová. *Study of optical amplification in silicon based nanostructures*. PhD thesis, Université Louis Pasteur - Strasbourg I, 2007.
- [11] J. Valenta, I. Pelant, and J. Linnros. Waveguiding effects in the measurement of optical gain in a layer of si nanocrystals. *Applied Physics Letters*, 81(8), August 2002. [doi:10.1063/1.1502195](https://doi.org/10.1063/1.1502195).
- [12] Eva Skopalová. Mode Structure in the Light Emission from Planar Waveguides with Silicon Nanocrystals. Master's thesis, Charles University, 2007.
- [13] O. Svelto, S. Taccheo, and C. Svelto. Analysis of amplified spontaneous emission: some corrections to the Linford formula. *Optics Communications*, 149(1998):277–282, April 1998. [doi:10.1016/S0030-4018\(98\)00054-6](https://doi.org/10.1016/S0030-4018(98)00054-6).

- [14] L. Dal Negro, P. Bettotti, M. Cazzanelli, D. Pacifici, and L. Pavesi. Applicability conditions and experimental analysis of the variable stripe length method for gain measurements. *Optics Communications*, 229(2004):337–348, 2004. doi:[10.1016/j.optcom.2003.10.051](https://doi.org/10.1016/j.optcom.2003.10.051).
- [15] OriginLab Corporation. Origin C programming, 2011. Available from: <http://www.originlab.com/index.aspx?go=Products/Origin/Programming/OriginC>.
- [16] OriginLab Corporation. The Smooth Dialog Box, 2011. Available from: http://www.originlab.com/www/helponline/Origin/en/UserGuide/The_Smooth_Dialog_Box.html.

A Optical Gain Analysis Toolkit

In this appendix I will describe a collection of algorithms and subroutines that I wrote to simplify and accelerate data processing during this project. All the graphs and plots included in the main report were generated by subroutines in this collection, which I dubbed [the] “OPTICAL GAIN ANALYSIS TOOLKIT” (OGAT). As of this writing (version 0.9.1, dated 19-07-2011), it comprises roughly thirty subroutines and helper procedures in nearly 1600 lines of code, and is available on request from the author.

The OGAT was written in Origin C, a semi object-oriented programming language created by OriginLab Corporation for use with their data analysis and graphing software [Origin](#), and is meant to be used from within that same software. It is based on the popular programming languages C++ and C# [15], and is therefore easy to learn for anyone versed in either of those two languages. Origin comes with its own Integrated Development Environment (IDE) in which users can write and test their code, but I used [Microsoft Visual C++ Express](#) for this purpose, because it has a feature called ‘[IntelliSense](#)’ that simplifies the development process.

The toolkit consists of three main interface dialogs—the main toolkit dialog (`OGAT_DLG_Toolkit`) and two auto-processing dialogs (`OGAT_DLG_Import` and `OGAT_DLG_Worksheets`), accessible through three custom toolbar buttons. The main toolkit dialog provides visual access to all the algorithms and subroutines that make up the toolkit, and can be used to manually perform the processing steps that are handled automatically by the auto-processing dialogs, as well as for a host of other tasks. The `Import` auto-processing dialog allows the user to select a list of raw VSL and SES data files—or a folder containing such—and to specify a number of parameters to be used during processing. The `Worksheets` dialog, as the name suggests, allows the user to select worksheets containing raw VSL and SES data, and to specify a number of parameters. Both dialogs perform automatic processing of the selected data according to the specified parameters, the end result of which will be a contour map of the differences between normalized VSL and integrated SES data, plotted against stripe length and wavelength (e.g. Fig. 4.11).

A.1 Main toolkit dialog

The main toolkit dialog, as explained above, provides visual access to the toolkit’s collection of algorithms and subroutines. This allows the user full control over all processing steps, which can be applied to all columns of the active sheet in any order. As shown in Fig. A.1, the dialog is divided into ten separate sections (called *branches* in Origin): `General parameters`, `Pre-/Post-processing`, `Smooth data`, `Reduce data`, `Normalize data`, `Sheet math`, `Find & plot specific column`, `Contour plot` and `Sheet deleter`. Aside from the first branch, each section has its own `Apply` button (or `Generate` in the case of the plot branches), which is used instead of the `OK` button at the bottom to execute a specific processing step. The different sections are explained in detail below. Some of the functionality provided by the toolkit is already available through Origin’s own dialogs, but in most cases can only be applied to a single column of data at a time, where the operations in this toolkit are applied to every (Y) column in the active worksheet. Note: due to certain limitations, it is not possible to open the main toolkit dialog when the active window is not a workbook or graph. Even when the active window is a graph, the dialog can only be used when a worksheet is associated with it in some way.

A.1.1 General parameters

In this branch the user can specify a number of parameters to be used by the other branches. Most are self explanatory, but will be described briefly anyway.

Put generated data in Specifies where to put newly generated data; in a new worksheet inside the current book, in a new workbook, or overwriting existing data. Note: this parameter is ignored by the following branches; `Normalize data` (option `Linear regression` only), `Find & plot specific column`, `Sheet deleter` and `Contour plot` (using `virtual matrix`).

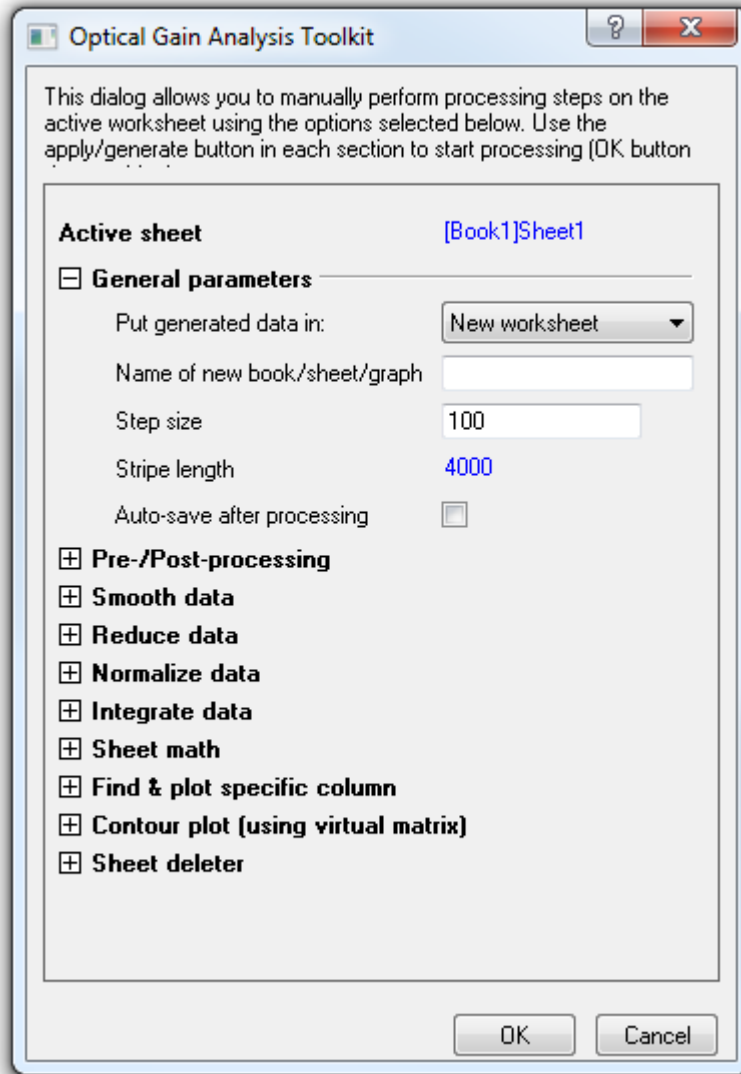


Figure A.1: A screenshot of the main toolkit dialog with the **General parameters** branch expanded.

The first always overwrites existing data, the second and third do not generate any new data and the last uses a virtual matrix as its data store.

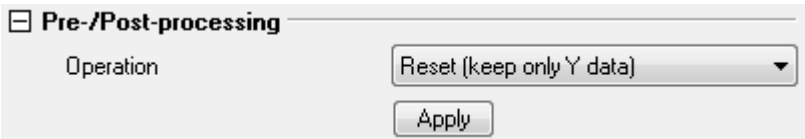
Name of new book/sheet/graph Name of the newly generated object.

Step size VSL and SES step size. This parameter is also used to generate X scales in most other branches, which is why it can be found in this section.

Stripe length VSL stripe length / SES end position. This parameter is calculated automatically based on the step size and the number of Y columns in the active sheet, and is displayed here for informational purposes only.

Auto-save after processing Check this to enable automatic saving of the project when processing is complete.

A.1.2 Pre-/Post-processing



This branch only has a single parameter: **Operation**. Possible choices are explained below.

Trim empty rows & columns Trims (removes) all empty rows and columns from the worksheet. Note: empty rows are only deleted from the end, not from the middle or from the beginning.

Reset Removes X column, if present (only if it is the first column) and resets all labels to empty.

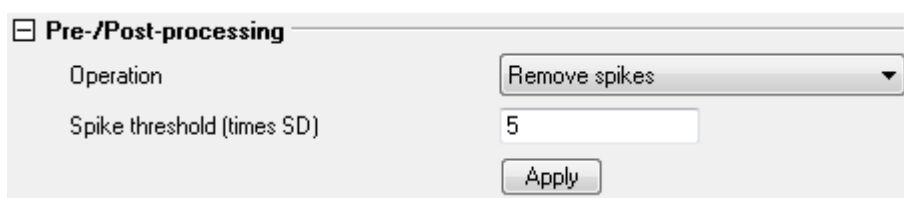
Raw Intended to be applied to a worksheet after importing raw data, it sets the first column as Y, adds an X column filled with values based on the `OGAT_PixelToWLstr` formula, adds labels to every column and resizes the sheet.

VSL Intended to be applied to (reduced) VSL data, it transposes the data, adds an X column filled with values based on the `Step size` parameter, adds labels to every column and resizes the sheet.

SES Intended to be applied to (reduced) SES data, it does exactly the same as the VSL option, except that some of the labels are different.

IntSES Intended to be applied to integrated SES data, it does exactly the same as the previous two options, except that it does not transpose the sheet and some of the labels are different.

Remove spikes Intended to be applied to raw data, it attempts to remove any spikes (i.e. data points exceeding a specified number of times the standard deviation of a column) from the input data. When this operation is selected, a new parameter appears: **Spike threshold (times SD)**. This parameter specifies the number of times a particular value has to exceed the standard deviation of the corresponding range before being detected and removed by this operation. Users should always check their data manually after applying this function, because it might remove useful data (especially if the threshold is set too low), or it might not detect all spikes.



A.1.3 Smooth data

This branch allows the user to smooth all data in the active worksheet, using the selected method. Input parameters vary depending on the method selected. For more information, please refer to the [Origin C Reference](#) or the section about The Smooth Dialog Box[16] in the Origin Reference (Help). Be advised that in the Origin Reference a few parameters have different names: **Median filtering** is called **Percentile filter**, **Weight smoothing** is called **Weighted Average** and **Pad edges** is called **Boundary Condition**. Note: the FFT filter method is not available from within the toolkit. Available methods are (descriptions adapted from [16]):

Adjacent averaging This method takes the average of a certain number (`Window size`) of data points around each point in the data and replaces that point with the new average value.

Smooth data

Window size	20
Method	Adjacent averaging
Pad edges	Repeat
Weight smoothing	<input type="checkbox"/>
Apply	

Savitzky-Golay This method performs a local polynomial regression. It is best suited to remove noise without affecting the overall signal shape. Original data values are replaced with fitted values.

Smooth data

Window size	20
Method	Savitzky-Golay
Pad edges	Repeat
Points used for convolution	-1
Note: a value of -1 means use the Window size value	
Polynomial degree	2
Derivative order	0
Apply	

Median filtering This method is also known as rank-order filter. It locates the specified percentile of data points in the data window around each point in the data and replaces that point with the percentile. It is best suited for removing shot noise.

Smooth data

Window size	20
Method	Median filtering
Pad edges	Repeat
Median filter %	50.00
Average smoothing	<input type="checkbox"/>
Apply	

A.1.4 Reduce data

Reduce data

For every .. rows	16
Keep only	Mean
Apply	

This branch allows the user to reduce the number of rows in the worksheet by merging data points. It has two parameters; the first specifies the number of data points to be merged into a single data point and the second specifies which value to keep while merging. There are ten different options

available, all of which are self explanatory and shall not be further explained here. For example, **Mean** keeps only the average value of every [first parameter] number of data points. Other options include **Min**, **Max**, **Median**, **First**, **Middle**, **Random**, **Last**, **Sum** and **Std. Dev.**.

A.1.5 Normalize data

Normalize data

Operation	Divide by specified value
Value	2
Apply	

This branch allows the user to normalize data by applying the specified operation, most of which are self-explanatory. The parameter **Value** is only available when either the **Divide by specified value** or the **Add specified value** operation is selected. A special case is the **Linear regression** operation, which will be explained in detail below. Other operations are: **Normalize to {0, 1}**, **Divide by max**, **Divide by abs max**, **Divide by min**, **Divide by abs min**, **Divide by mean**, **Divide by median**, **Divide by std. dev.**, **Divide by norm**, **Divide by mode** and **Divide by sum**.

Linear regression This operation is intended to correct for oversampling during SES measurements (i. e. if the SES spot size is larger then the step size). It performs a linear fit [$y = a+bx$] on the first few data points (assuming both VSL and integrated SES curves are linear there) and subtracts the calculated ‘a’ parameter from both datasets independently. This procedure should correct for any constant background noise. It then multiplies the data in the second sheet (i. e. integrated SES data) by the calculated ‘b’ parameter from the linear fit of the VSL data and divides that same data by the ‘b’ parameter from the fit of the integrated SES data. If you were to plot the same column from both sheets in a single graph after performing this operation, the curves would be on top of each other for the first few points—as they should be in an ideal situation. Any rows or columns outside the range of one of the sheets will be ignored.

Normalize data

Operation	Linear regression
Worksheet 1 (columns - lr1.a)	[Book1]Sheet1
Worksheet 2 ((columns - lr2.a) * lr1.b / lr2.b)	
Use first ... data points	5
Enable noise filter (experimental)	<input type="checkbox"/>
X range	Increment by Step size
Apply	

Parameters that can be specified for the linear regression operation are: **Worksheet 1** (i. e. the VSL sheet), **Worksheet 2** (i. e. the integrated SES sheet), the number of data points to use for the fit (starting from the beginning), **Enable noise filter** and **X range**. When the noise filter is enabled, all columns that end up with a negative slope (or ‘b’ parameter) will be ignored. Since neither VSL nor integrated SES data should ever be negative, enabling this option will filter out any noise caused by faulty fits. Finally, the **X range** parameter controls how to calculate the X values to be used during regression. Options are: **Row numbers**, **From sheet** and **Increment by Step size**. The first option uses row numbers for X values; the second option uses the X column of the first sheet if available, or the X column of the second sheet if available, otherwise it falls

back to using row numbers; the third option generates X values starting from 0 and increasing by the `Step size` parameter for every new row.

A.1.6 Integrate data

Integrate data

Operation	Cumulative sum
<input type="button" value="Apply"/>	

This branch allows the user to integrate all data numerically. It takes a single parameter, `Operation`, but at the time of this writing it only allows one option: `Cumulative sum`. When applied to a sequence (e.g. $\{a, b, c, \dots\}$), this operation calculates the sum of all the previous values up until the current point (e.g. $\{a, a + b, a + b + c, \dots\}$).

A.1.7 Sheet math

Sheet math

Worksheet 1	[Book1]Sheet1
Worksheet 2	
Operation	Subtract
<input type="button" value="Apply"/>	

This branch allows the user to perform simple mathematical operations to entire sheets at once. It takes three parameters: `Worksheet 1`, `Worksheet 2` and `Operation`. Usage is self-explanatory; for example, when selecting `Add`, all values from every column in the first worksheet will be added to the corresponding values in the same column of the second worksheet. Any rows or columns outside the range of one of the sheets will be ignored.

A.1.8 Find & plot specific column

Find & plot specific column

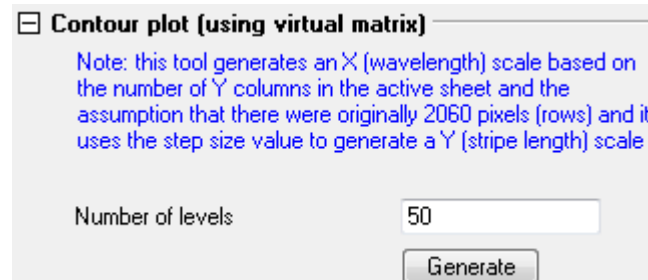
Note: search is case sensitive. Also pay attention to the decimal separator when searching for a number; text fields like comments may have a dot, while first row values may have a comma, depending on the language settings

Search for	
in	Comments
of sheet	[Book1]Sheet1
Search mode:	Starts with
Add to plot	<New>
Automatic line coloring	<input checked="" type="checkbox"/>
Note: enabling automatic line coloring will disregard any existing color settings	
Rescale	<input checked="" type="checkbox"/>
Update legend	<input checked="" type="checkbox"/>
<input type="button" value="Generate"/>	

This branch allows the user to, as the name suggests, find and plot a specific column in the specified worksheet. Again, most parameters should not require any explanation. Possible search locations

include: **Comments**, **Short name**, **Long name** and **First row**. Search mode refers to the method used when comparing the search string with the value of the specified location, and can be any of the following: **Equals**, **Starts with** (i.e. search string matches the start of the value under consideration), **Ends with** and **Contains**. Any existing plot can be chosen to which to add the columns matching the criteria, or a new graph window can be created. When a new plot is created, that plot will automatically be selected the next time. Enabling **Automatic line coloring** will set reset all colors in the graph to predetermined values (there are 23 different colors in the default palette, excluding white). When **Automatic line coloring** is disabled, added curves will have the default color black, but existing colors will not be replaced. The plot will be rescaled and the legend updated after each addition, if the corresponding checkboxes are ticked.

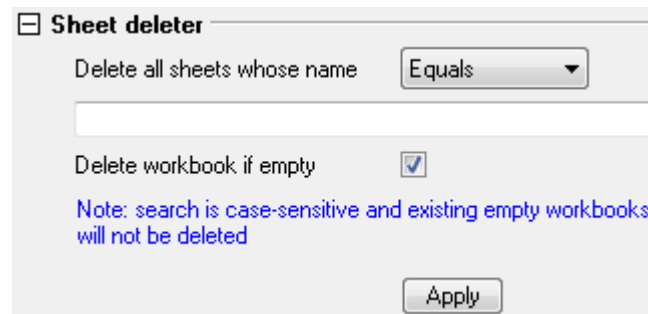
A.1.9 Contour plot



This branch allows the user to generate a contour map of the data in the active worksheet, using a virtual matrix as a data store. The X and Y scales will be generated automatically, as described in the note (see image). Creating this type of contour plot directly from a worksheet is one of the new features of Origin 8.5 and has certain advantages. However, it is likely that the method used by this toolkit will also function in previous versions of Origin, contrary to the built-in method, although this has not been tested yet. For more information about this type of contour plot, please refer to the [relevant section](#) of the Origin 8.5 user guide.

There is one parameter, **Number of levels**, which specifies the number of contour levels to generate. Note: due to certain limitations, the toolkit does not currently generate accurate color maps (i.e. although the number of colors is set correctly, there will only be ten different colors displayed initially). A workaround is to double-click the map, double click the **Level...** column header, click **OK** and click **OK** again. This will make Origin generate a new color map based on the specified number of levels.

A.1.10 Sheet deleter



This branch allows the user to find and delete worksheets whose name matches the specified criteria. Possible search modes are the same as those in the **Find & plot specific column** branch. If any workbooks are left empty as a result of this operation, they can optionally be deleted as well.

A.2 Import auto-processing dialog

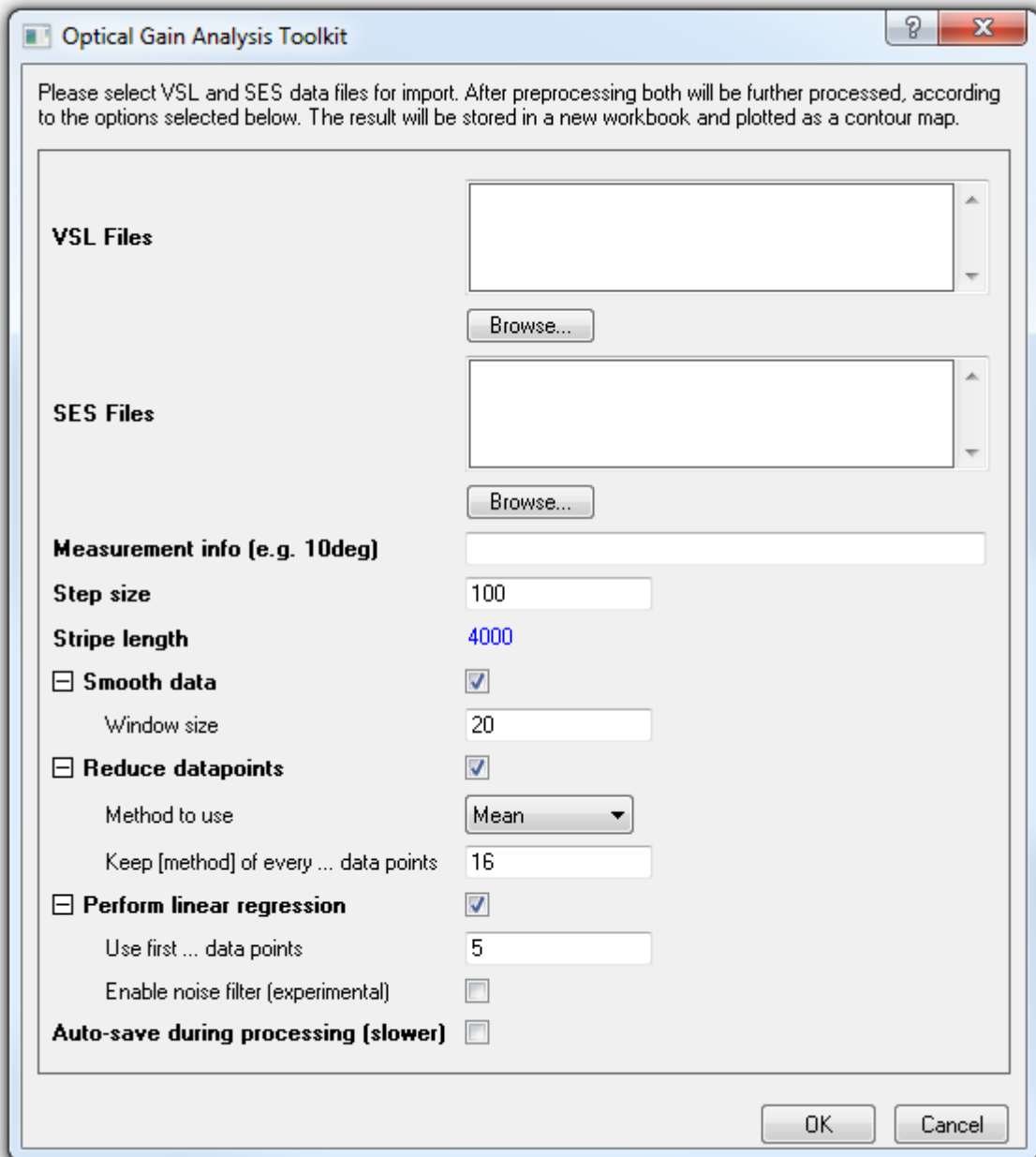


Figure A.2: A screenshot of the **Import** auto-processing dialog, fully expanded.

The **Import** auto-processing dialog, as explained above, allows the user to select a list of raw VSL and SES data files and to specify a number of parameters to be used during processing. After importing all files into the columns of two separate worksheets, processing occurs according to the procedure described in the main text. The imported data will optionally be smoothed, reduced and normalized using the linear regression method, according to the user's choices. The end result will be a contour map detailing the differences between VSL and integrated SES data, plotted against wavelength (X) and stripe length (Y). The different parameters are described in detail below.

VSL Files Specify a list of ASCII files containing raw VSL data (i.e. PL spectra at various stripe lengths, as generated by the C7557-01 CCD application), here. Clicking the **Browse...** button will open a dialog allowing the user to select these files as usual.

SES Files Same as **VSL Files**, but for files containing raw SES data.

Measurement info Any text specified in this field will be appended to the names of generated workbooks and graph windows. Use this to add any useful info pertaining to the current selection of files.

Step size VSL and SES step size. This parameter is used to generate **X** scales.

Stripe length VSL stripe length / SES end position. This parameter is calculated automatically based on the step size and the number of selected files, and is displayed here for informational purposes only.

Smooth data When this branch is selected, imported data is smoothed using the **adjacent averaging** method and the specified smoothing **window size**, before being processed. Refer to section A.1.3 for more information.

Reduce datapoints When this branch is selected, imported data is reduced using the parameters specified, before being processed. Refer to section A.1.4 for more information.

Perform linear regression When this branch is selected, preprocessed data is normalized using the linear regression method and the specified parameters, as described in section A.1.5.

Auto-save during processing When this option is checked, the project will automatically be saved at several key points during processing. Enabling this significantly reduces processing speed and is therefore not recommended. Usually, processing should be fast enough that having to redo it if something goes wrong should not be much of a problem, so it is safe to leave this option unchecked.

Clicking the **OK** button will start automatic processing. Processing can be aborted at any time by pressing the **Esc** key.

A.3 Worksheets auto-processing dialog

The **Worksheets** auto-processing dialog, as explained above, allows the user to select worksheets containing raw VSL and SES data, and to specify a number of parameters to be used during processing. Processing occurs according to the procedure described in the main text. The data in the selected worksheets will optionally be smoothed, reduced and normalized using the linear regression method, according to the user's choices. The end result will be a contour map detailing the differences between VSL and integrated SES data, plotted against wavelength (**X**) and stripe length (**Y**). The different parameters are the same as those described in the previous section, except for **Start processing in**. The latter is similar to the option **Put generated data in** from the main toolkit dialog and allows the user to specify what to do with existing (raw) data in the selected worksheets, which can either be overwritten, copied to a new worksheet or copied to a new workbook before processing. Please refer to section A.2 for a detailed description of the other parameters.

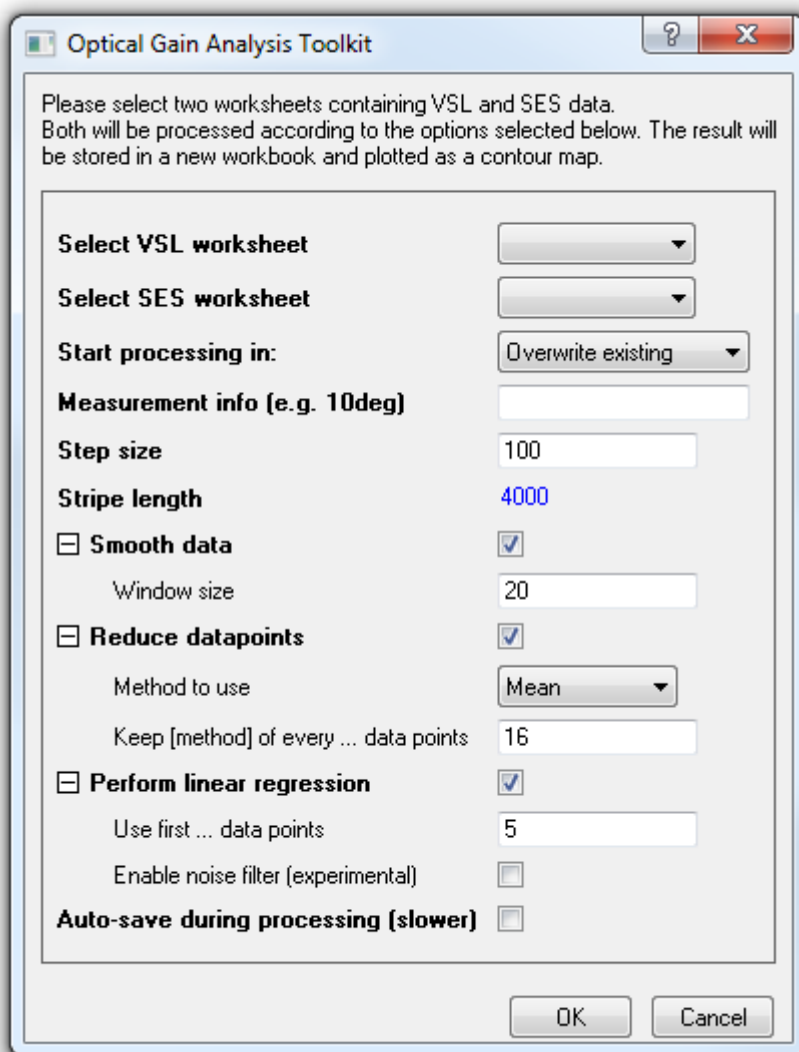


Figure A.3: Screenshot of the Worksheets auto-processing dialog, fully expanded.